Title

Astrocytic Integration of Histaminergic Signaling in the Cortex

Author

Taylor, Charlotte R

Publication Date

2024

Astrocytic Integration of Histaminergic Signaling in the Cortex

by
Charlotte Rhiannon Taylor

DISSERTATION
Submitted in partial satisfaction of the requirements for degree of
DOCTOR OF PHILOSOPHY

in

Neuroscience

in the

GRADUATE DIVISION
of the
UNIVERSITY OF CALIFORNIA, SAN FRANCISCO

Approved:

DocuSigned by:
Anna Victoria Molofsky
7148719D502F43A...

Anna Victoria Molofsky
Chair

DocuSigned by:
Graeme Davis
Signed by:DF89F4A3...

Graeme Davis

DocuSigned by:
Felice Dunn
[illegible]405...

Felice Dunn

DocuSigned by:
Jeanne Paz
[illegible]445...

Jeanne Paz

DocuSigned by:
Kira Poskanzer
64ED3BCFD209496...

Kira Poskanzer

Committee Members

ACKNOWLEDGEMENTS

I extend my sincere gratitude to my past and present mentors. First, thank you to my undergraduate mentors at the University of Oregon — Judith Eisen, Julia Ganz, and Ellie Melancon. You three inspired my passion for research and led by impeccable example. Thank you to my mentors at the University of California, Berkeley, who gave me the confidence to continue my scientific pursuits: Richard Kramer, Christopher Davenport, Rajit Rajappa, and Mei Li.

My wholehearted appreciation to those who have led me through this PhD. Thank you to my primary mentor, Kira Poskanzer, who offered continued guidance and weekly check-ins even after starting on her new path at Arcadia Science. My sincere thanks to Jeanne Paz, who stepped in as a secondary mentor offering critical advice and support after Kira's departure. Thank you to all those on my qualifying and thesis committees — I learned a great deal from you: Grae Davis, Anna Molofsky, Kevin Bender, and Roshanak Irannejad, and a special thank you to Felice Dunn who provided thoughtful support in difficult moments. To past and present Poskanzer lab members, thank you for your technical guidance, comradery, and genuine encouragement.

To my sweet friends: there are too many of you to name here, but if we discussed my PhD progress over the years, thank you. Your confidence in me made this possible.

Finally, thank you to my dear friend, Teresa Puthussery, and to my parents, Rowland Taylor and Catherine Morgans. I am so lucky to have three incredible scientific mentors within my own family. I've learned so much from watching each of you work in your own way. Thank you for your constant, steadfast support.

CONTRIBUTIONS

Work presented in Chapters 2 and 3 is reprinted and modified content that appears in the following publications:

1. Taylor CR, Tse V, Willoughby DD, Levesque M, Vaidyanathan TV, Paz JT, Poskanzer KE. (2024) Histamine-1-receptors regulate cortical astrocyte Ca^{2+} and extracellular adenosine dynamics during REM sleep. [Manuscript in submission].

2. Pittolo S, Yokoyama S, Willoughby DD, Taylor CR, Reitman ME, Tse V, Wu Z, Etchenique R, Li Y, Poskanzer KE. Dopamine activates astrocytes in prefrontal cortex via α1-adrenergic receptors. Cell Rep. 2022 Sep 27;40(13):111426. doi: 10.1016/j.celrep.2022.111426. PMID: 36170823; PMCID: PMC9555850.

Kira E Poskanzer and Charlotte R Taylor designed the study presented in Chapters 1–4. Charlotte R Taylor collected and analyzed data presented in Chapter 2, except for data analysis and figure design shown in Figure 2.4.9, which were completed by Silvia Pittolo and included in Pittolo et al., 2022. *In vivo* data in Chapter 3 was collected by Vincent Tse and Drew D Willoughby. Sleep scoring presented in Chapter 3 was done using a Hidden-Markov Model customized by Drew D Willoughby with input from Maxine Levesque, subsequent data analysis was done by Charlotte R Taylor. Kira E Poskanzer provided feedback on writing and data presentation in Chapters 1–4. Throughout the dissertation, ChatGPT was used to edit writing syntax.

ASTROCYTIC INTEGRATION OF HISTAMINERGIC SIGNALING IN THE CORTEX

Charlotte R. Taylor

ABSTRACT

Finely tuned arousal control is required for animal survival. To catch food, a predatory animal is keenly attentive on a hunt, and to survive, prey is acutely vigilant. These critical attentional dynamics require sufficient sleep, which promotes optimal neuronal function by facilitating waste clearance, metabolic homeostasis, and immune regulation[1,2]. In humans, disordered sleep is associated with attentional and cognitive deficits, increased risk of accident, disease, and psychiatric disease, underscoring the importance of unravelling the cellular mechanisms underlying the balance of sleep and wake[3–5]. That said, our understanding of arousal control is mostly limited to neuronal studies, leaving the role of non-neuronal brain cells largely unknown.

Classical neuromodulators regulate arousal states, spanning deep sleep to vigilant wakefulness, primarily by activating cortical neurons[1,6,7]. However, cortical astrocytes also express neuromodulatory G-protein coupled receptors (GPCRs)[8,9]. While astrocytic noradrenergic receptors can modulate two critical regulators of arousal—cortical synchrony[10] and extracellular adenosine levels[11–14]—how other neuromodulatory signaling pathways similarly shape arousal remains unclear. Astrocytes in mammalian cortex express particularly high levels of the wake-promoting histamine-1-receptor (H1R) GPCR[8], yet little is known about how astrocytic H1R contributes to regulation of arousal.

To address this gap, we used pharmacological and genetic approaches in murine cortex to test how astrocytic H1R signaling affects astrocyte Ca^{2+}, cortical activity across sleep/wake, and release of adenosine—an output of astrocytic activity known to promote sleep. Using *ex vivo* two-photon Ca^{2+} imaging in acute cortical slices, we show that H1R activation drives cell-autonomous astrocyte Ca^{2+} elevations and stimulates release of ATP, which is extracellularly metabolized to adenosine. In a parallel project published by Silvia Pittolo et al.[15], we show that DA also triggers ATP release in the cortex, suggesting that a critical function of astrocyte-neuromodulatory signaling may be to increase cortical ATP/adenosine levels. Next, *in vivo* fiber photometry and electrophysiology results show that astrocyte-specific H1R deletion in cortex disrupts local astrocyte Ca^{2+} and extracellular adenosine dynamics specifically around rapid eye movement (REM) sleep transitions, when HA release is minimal. We observe concurrent changes in cortical oscillations during REM, suggesting that H1R activation, during wake when HA is released, induces lasting changes in astrocyte physiology to modulate extracellular adenosine and cortical dynamics in REM sleep. These findings contribute to an emerging model in which astrocytes integrate neuromodulators on a minutes-long timescale to regulate sleep/wake neuronal dynamics via adenosine signaling.

Abstract is adapted from:

Taylor CR, Tse V, Willoughby DD, Levesque M, Vaidyanathan TV, Paz JT, Poskanzer KE. (2024) Histamine-1-receptors regulate cortical astrocyte Ca^{2+} and extracellular adenosine dynamics during REM sleep. [Manuscript in submission].

Table of Contents

List of Figures

CHAPTER 2

CHAPTER 3

CHAPTER 4

List of Abbreviations

HA	histamine
H1R	histamine-1-receptor
TMN	tuberomammillary nucleus
NE	norepinephrine
Adra1a	alpha-1A-adrenergic receptors
ACh	acetylcholine
DA	dopamine
V1	visual cortex
mPFC	medial prefrontal cortex
GPCR	G-protein coupled receptor
SWA	slow wave activity
EEG	electroencephalogram
EMG	electromyogram
REM	rapid eye movement
NREM	non-rapid eye movement
ATP	adenosine triphosphate
2P	two-photon
AQuA	Astrocyte Quantitative Analysis software
ACSF	artificial cerebrospinal fluid
TTX	tetrodotoxin

CHAPTER 1

INTRODUCTION TO ASTROCYTIC AROUSAL CONTROL

Astrocytes, the most numerous glial subtype in the mammalian central nervous system, have been implicated in regulation of cortical arousal across sleep/wake[16]. These cells express receptors for major sleep/wake regulatory neuromodulators including norepinephrine (NE), acetylcholine (ACh), and histamine (HA)[16], which promote arousal during the wake state[3,17,18]. Thus, astrocytes have been hypothesized to contribute to arousal control via integration of neuromodulators. However, our understanding of how astrocyte-neuromodulatory signaling contributes to arousal control has largely not expanded beyond noradrenergic studies, despite astrocytic expression of receptors for other neuromodulators[8,9]. **This dissertation investigates how astrocyte-specific HA receptors shape astrocyte physiology, and demonstrates that astrocytes integrate HA input on a minutes-long timescale to regulate molecular determinants of sleep/wake behavior.**

1.1 CORTICAL CONTROL OF SLEEP/WAKE

Physiological brain states in mammals, spanning deep sleep to vigilant wakefulness, are defined by unique cortical activity patterns that modulate cognitive processing[3]. Non-rapid eye movement (NREM) sleep is characterized by highly synchronized neuronal firing manifesting as low frequency (0.5–4 Hz), high amplitude electrical activity across the cortex, termed slow wave activity (SWA). The wake state is characterized by increased and desynchronized neuronal firing manifesting as high frequency, low amplitude cortical activity[3]. Within wakefulness, different levels of arousal are characterized by shifts in cortical oscillatory dynamics; for example, quiet wakefulness is characterized by an increased in low frequency (<10 Hz) power[19]. During attentive

wake, such as after a foot shock or in the presence of a predator, low frequency power decreases and high frequency power increases. This increase in cortical arousal is thought to underlie increased cognitive performance, thereby promoting learning and animal survival[19]. Mammals exhibit a third major brain state, rapid eye movement (REM) sleep, which is characterized by zero muscle tone, but increased cortical activity as seen during wakefulness and increased oscillatory power in the theta frequency band (6–10 Hz)[3].

The dynamics of wake, NREM, and REM can be understood via a three-part model: the circadian clock, sleep homeostat, and sleep/wake switch[17]. In this model, circadian rhythms and the sleep homeostat control the likelihood of sleep onset and sleep depth, both of which increase with sleep pressure that builds throughout an animal's active phase[20]. The transitions from wake to sleep are triggered by the sleep/wake switch. These three model components are controlled by distinct, interconnected brain regions including the cortex, thalamus, hypothalamus, basal forebrain, brainstem, and monoaminergic subcortical nuclei that each release distinct transmitters[1]. I will focus only on the role of the cortex and subcortical neuromodulatory nuclei, because these regions are most relevant to work presented here. For the sake of simplicity, I will highlight the primary sleep/wake regulatory functions that have been experimentally linked to these brain regions. However, it is important to note that sleep/wake regulatory brain regions are highly interconnected, making it difficult to exclusively assign certain functions to distinct regions.

The cortex is where sleep/wake states are instantiated and is thought to contribute to both the sleep/wake switch and sleep homeostasis. The role of cortex in the sleep/wake switch is relatively simple – increased cortical arousal is required for the transition from sleep to wake. In fact, direct cortical stimulation is sufficient to wake up an animal from sleep[21]. Neuronal dynamics in cortex also characterize sleep homeostasis, as cortical SWA during NREM

homeostatically increases with time awake[1,22–24]. The idea that cortex might be the control center for homeostatic changes in NREM SWA is indicated by multiple lines of evidence. First, *ex vivo* slabs of cortex spontaneously generate slow neuronal oscillations analogous to SWA[25]. Additionally, extracellular adenosine dynamics in cortex regulate homeostatic increases in SWA[26,27]. Microdialysis experiments have shown that cortical extracellular adenosine levels increase with time awake and decrease during sleep[28], and direct application of adenosine in cortex increases SWA[29] and induces NREM sleep[30,31], demonstrating that SWA can be locally regulated by adenosine signaling in cortex. What remains unclear are the cellular mechanisms underlying cortical fluctuations in extracellular adenosine and whether cortical adenosine is required for sleep homeostasis. Overall, shifts in cortical activity are fundamental to sleep and wake states, and can be regulated via local mechanisms, specifically via changes in extracellular adenosine.

Subcortical neuromodulatory nuclei functionally contribute to the sleep/wake switch by promoting cortical arousal at sleep-to-wake transitions and within the wake state. Each neuromodulatory nucleus projects axons throughout the cortex, and releases either a monoamine, (HA, NE, dopamine (DA), serotonin), or ACh[6]. These transmitters are largely volumetrically released[32], rather than synaptically, and generally increase desynchrony in the cortex by shaping excitability and synaptic release probabilities in cortical neurons[1,6,33]. The wake-promoting effect of these neuromodulators is demonstrated by pharmacological experiments in which the blockade of specific neuromodulatory G-protein coupled receptors (GPCR)—such as alpha-1A-adrenergic receptors (Adra1a), histamine-1-receptor (H1R), or muscarinic receptors—results in reduced cortical desynchronization (indicative of decreased arousal) and increased NREM sleep[22]. Additionally, activation of certain neuromodulatory receptors, such as Adra1a, increases

discrimination task performance and the gain of sensory perception during wake[34], suggesting that these neuromodulators promote cortical desynchrony to enhance cognitive processing during wakefulness[7].

Our current mechanistic understanding of how these neuromodulators shape cortical activity is based on neuronal studies showing that activation of neuromodulatory GPCRs shapes neuronal excitability in cortex. However, neurons are not the only cortical cell type expressing neuromodulatory GPCRs. Glia—which include astrocytes, oligodendrocytes, and microglia—also express these receptors, and in some cases express them at higher levels than neurons[8,9]. Yet, how activation of glial neuromodulatory GPCRs contributes to brain-state dynamics remains largely unknown.

1.2 ASTROCYTES ARE POISED TO INTEGRATE NEUROMODULATORS

Of the glial subtypes, astrocytes appear particularly well poised to facilitate the circuit-wide shifts in cortical activity triggered by neuromodulators[35,36]. First, an individual astrocyte contacts > 100,000 synapses while forming a continuous network with neighboring astrocytes via gap-junctions[16], thus they are tuned to neuronal activity levels and potentially able to communicate changes in synaptic activity across the astrocyte syncytium. Second, astrocytes regulate extracellular neurotransmitter levels, buffer extracellular K^+, release the neuromodulators adenosine and d-serine, and control neuronal metabolism, processes that significantly shape neuronal dynamics[16]. Finally, cortical astrocytes respond to many neuromodulators with Ca^{2+} elevations[16,35,36], although the mechanistic details of these responses are not completely described. Therefore, astrocytes can listen to both nearby synapses and long-range neuromodulatory signals, potentially integrate these signals via Ca^{2+} signaling, and ultimately modulate neuronal activity

patterns via changes in neurotransmitter uptake, K^+ buffering, neuromodulator release or astrocyte-neuron metabolic coupling. This idea is supported by multiple studies showing that manipulation of *in vivo* astrocyte Ca^{2+} dynamics leads to shifts in cortical arousal and sleep/wake architecture[37]. However, elucidating the functional role of neuromodulatory GPCR signaling in astrocytes, and whether it significantly contributes to cortical state control, is limited by a lack of studies using astrocyte-specific manipulations.

Our understanding of how astrocytes respond to neuromodulators is almost exclusively informed by noradrenergic studies, which support the broad hypothesis that astrocytes integrate neuromodulatory signals to regulate cortical arousal. NE has been shown to drive *in vivo* astrocyte Ca^{2+} via astrocyte-specific Adra1a[10,38–40]. The functional significance of this relationship is demonstrated by an astrocyte-specific knockout study by Reitman et al., which showed that NE-triggered astrocyte Ca^{2+} precedes cortical resynchronization events after moments of acute arousal, and that cortical resynchronization is reduced after astrocyte-specific deletion of Adra1a in cortex[10]. While the underlying Ca^{2+}-dependent astrocyte output mediating this effect is unclear, it is consistent with *ex vivo* and *in vivo* studies demonstrating that electrophysiological[41], optogenetic[42], or chemogenetic[43] stimulation of astrocyte Ca^{2+} leads to increased neuronal synchrony in cortex. Finally, several studies have shown that astrocytic Adra1a signaling drives adenosine release[11,12,14], which is known to increase cortical SWA[44]. Together, these observations establish a precedent for astrocytes integrating neuromodulators to regulate cortical arousal and, consequently, contribute to sleep/wake regulation.

Astrocytes are known to express many other neuromodulatory GPCRs in addition to adrenergic receptors, but we know very little about how these non-adrenergic receptors on astrocytes contribute to arousal regulation by neuromodulators. Thus, other neuromodulators should be

studied in the context of astrocyte physiology to reveal the complete picture of how astrocyte-neuromodulatory signaling contributes to brain state regulation.

1.3 ASTROCYTIC SLEEP/WAKE REGULATION

While the function of astrocyte-neuromodulatory signaling in arousal control remains an active area of study, it is well established that astrocytes track and regulate arousal dynamics[37,45]. Astrocytes are tuned to arousal dynamics in several ways. These cells exhibit distinct sleep- and wake-specific transcriptional profiles[46] and morphology changes across sleep/wake[47]. Astrocyte Ca^{2+} also fluctuates according to sleep/wake dynamics. In somatosensory, prefrontal, and visual cortex, astrocyte Ca^{2+} levels are positively correlated with arousal; Ca^{2+} activity ceases almost completely during NREM sleep and increases with wake-onset and when arousal increases within wake periods[43,48–50]. Perhaps due to the lack of NE release during REM, astrocytes in somatosensory and prefrontal cortices exhibit reduced Ca^{2+} in REM sleep[48,49], although it increases in other brain areas[51]. Overall, several lines of evidence—morphology, gene expression, and intracellular signaling—indicate that astrocyte physiology is tightly coupled to sleep/wake dynamics.

Consistent with the clear correlation between cortical astrocyte Ca^{2+} and arousal, targeted manipulation of astrocyte Ca^{2+} modulates cortical oscillations underlying sleep/wake. In neocortex, chemogenetically[43] induced astrocyte Ca^{2+} elevations increased cortical SWA during NREM sleep, and in *ex vivo* slice experiments, stimulation of astrocyte Ca^{2+} triggered neuronal oscillations analogous to SWA in NREM[41]. Consistent with these observations, attenuation of astrocyte Ca^{2+} activity, either via conditional STIM1 knockout or global IP3R2 knockout, reduced SWA activity after sleep deprivation[48] and during baseline NREM sleep[49], respectively. These

studies used relatively broad methods of Ca^{2+} manipulation, which could drive non-physiological changes in surrounding neuronal dynamics. However, more targeted astrocyte-specific knockout of Adra1a disrupts both astrocyte Ca^{2+} activity[52] and resynchronization of cortical activity after acute periods of increased arousal[10], reinforcing the idea that local astrocyte Ca^{2+} promotes neuronal synchrony in cortex, specifically SWA that characterizes NREM sleep, and further suggests that neuromodulatory input might drive this astrocyte-specific regulation.

The astrocytic outputs downstream of Ca^{2+} that mediate changes in arousal remain relatively unclear. However, several studies point to astrocytic regulation of extracellular adenosine as a key component of astrocyte mediated arousal control and neuronal regulation. In one study, astrocyte-specific deletion of adenosine kinase increased extracellular adenosine levels and SWA in wake and NREM sleep[53], which is consistent with increased delta power triggered by application of adenosine in cortex[29,31]. Separate studies suggest that genetic blockade of vesicular exocytosis in astrocytes also disrupts adenosine signaling leading to changes in SWA[54–56], although the astrocyte-specificity of genetic manipulations used in these studies has been challenged[57]. That said, several studies have shown that astrocytes release ATP via multiple mechanisms, including vesicular exocytosis[58–60] and transmembrane channels[61], and that wake-promoting neuromodulators trigger astrocytic ATP release[11,15,62]. Finally, two recent studies have demonstrated causal links between NE, astrocyte-Ca^{2+}, and neuronal modulation via adenosine. These studies used a combination of *ex vivo* and *in vivo* techniques in astrocyte-specific Adra1a knockouts to show that NE triggers Ca^{2+}-dependent ATP release from astrocytes, which leads to adenosine mediated neuronal inhibition in murine[12] and fish[14] brains. Thus, discrete lines of evidence together suggest that neuromodulators trigger astrocyte-adenosine signaling to regulate neuronal dynamics underlying sleep/wake. However, the direct links between these elements often

remain unclear, emphasizing the importance of investigating how individual neuromodulators distinctly shape astrocyte physiology—and specifically astrocyte-adenosine signaling—across sleep/wake.

1.4 HISTAMINERGIC SLEEP/WAKE REGULATION

Of the classical neuromodulators, HA release is particularly wake-specific[63–65]. Histaminergic neurons in the tuberomammillary nucleus (TMN), situated at the base of the hypothalamus, fire almost exclusively during wakefulness at < 10 Hz, and their firing rate shows a positive correlation with arousal level[66]. These histaminergic neurons project throughout the brain, including to the cortex[67]. HA promotes wakefulness primarily via activation of G_q-coupled H1R[68]. The wake-promoting effect of this receptor is demonstrated by drowsiness induced in humans by first-generation antihistamines, which can cross the blood-brain barrier to block H1R[69]. This is consistent with genetic knockout studies in mice, showing that H1R KO mice exhibit reduced arousal during wake and more NREM sleep, although this difference was observed only when knockout animals were presented with novel stimuli[70] or when HA release was pharmacologically increased[71], suggesting that other wake-promoting neuromodulatory systems are redundant or may compensate. Acute manipulation of histaminergic signaling, using optogenetics or pharmacology, has more clearly demonstrated the wake-promoting effect of HA. Optogenetic inhibition of TMN neurons leads to reduced arousal during wakefulness and more NREM sleep bouts[72], and pharmacological activation or blockade of H1R produced increased wakefulness and more NREM sleep, respectively[73]. Similar wake-promoting effects are seen when HA release is upregulated after pharmacological H3R blockade, which prevents autoinhibition of TMN neurons[71,74]. Currently, HA is thought to promote wakefulness by increasing neuronal excitability via H1R in

multiple waking-promoting brain regions including the cortex[64,68,75,76]. However, the primary cell types and brain areas mediating the wake-promoting effects of HA remain insufficiently characterized due to the limited number of localized cell-type specific H1R knockout studies.

Interestingly, cortical astrocytes express H1R at particularly high levels, higher than any other neuromodulatory GPCRs[8], including Adrα1a — a potent modulator of astrocyte physiology. This raises the question of whether H1R, like Adrα1a, significantly shapes astrocyte physiology and contributes to astrocytic regulation of arousal.

1.5 ASTROCYTE-HA SIGNALING ACROSS SLEEP/WAKE

Astrocytic expression of H1R was demonstrated in the 1980s[77]. Yet, very little is known about how HA modulates astrocyte physiology and whether astrocyte-HA signaling is important for sleep/wake regulation. Several early studies showed that astrocytes in culture and in brain slices can respond to HA via H1R with Ca^{2+} elevations[78]. However, the dose-dependency of these responses was poorly characterized, and whether cortical astrocytes responded to HA cell-autonomously was unknown—a particularly important gap to address since neurons also express H1R[9].

A study by Karpati et al. compared sleep/wake behavior in mice after down-regulation of astrocyte-specific or neuronal-specific H1R throughout the brain[79]. Down regulation of astrocytic H1R increased SWA activity during wake, an effect that was not seen after down regulating H1R specifically in neurons. This compelling result suggests that astrocytic H1R contributes to the waking-promoting effects of this receptor; however, several key questions remained unaddressed. First, is this effect driven primarily by astrocytes in a particular brain area? It is possible that astrocytic H1R deletion only in cortex is sufficient to drive decreased cortical arousal during wake.

Second, is astrocyte-specific H1R required for HA-triggered astrocyte Ca^{2+} activity, and if so, is H1R-mediated astrocyte Ca^{2+} linked to changes in arousal dynamics across sleep/wake? Finally, the astrocytic outputs downstream of H1R activation remained unclear.

1.6 SUMMARY

In Chapters 2 and 3, we address the questions outlined above by selectively deleting H1R in cortical astrocytes. This approach is combined with *ex vivo* and *in vivo* recording techniques to evaluate how astrocytic H1R deletion affects astrocytic Ca^{2+} activity, cortical arousal, and adenosine signaling across sleep/wake.

In Chapter 2, we use two-photon (2P) imaging in *ex vivo* neocortical slices to demonstrate that HA drives cell-autonomous, dose-dependent astrocytic Ca^{2+} elevations via H1R. We also show that astrocyte-specific H1R activation modifies subsequent Ca^{2+} responses to NE. This suggests that H1R stimulation triggers changes in astrocyte physiology that last many minutes, a timescale consistent with the idea that astrocyte Ca^{2+} during wake can shape cortical dynamics underlying NREM and REM sleep[43]. Finally, given that astrocytic regulation of adenosine signaling is linked to arousal control, we used 2P imaging of a fluorescent, extracellular-facing ATP sensor in the cortex to demonstrate that HA triggers an H1R-dependent increase in ATP release (the adenosine precursor). We found that ATP release increased many minutes after acute H1R stimulation, consistent with published data showing that astrocyte Ca^{2+} leads to many minutes delayed exocytosis of ATP[60,80,81].

In Chapter 3, we use *in vivo* fiber photometry and electroencephalography (EEG) recordings to test how astrocyte-specific H1R deletion affects astrocyte Ca^{2+}, cortical activity, and extracellular adenosine dynamics across sleep/wake. We show that astrocytic H1R deletion alters

in vivo astrocyte Ca^{2+} activity and extracellular adenosine dynamics in neocortex, with the most pronounced effects observed during REM sleep when HA is not released, suggesting that histaminergic signaling during wake has effects on astrocyte activity that persist beyond acute H1R activation. Finally, we see changes in delta power during REM sleep, indicating that astrocytic H1R signaling modulates cortical neuronal dynamics that characterize sleep.

Lastly, Chapter 4 synthesizes results from Chapters 2 and 3, and outlines future experiments to further illuminate how astrocyte-neuromodulatory signaling contributes to sleep/wake regulation.

CHAPTER 2

HA DRIVES ASTROCYTE CA^{2+} AND MODULATES ATP DYNAMICS IN CORTEX

2.1 INTRODUCTION

Manipulation of astrocyte Ca^{2+} activity can modulate neuronal dynamics[16]. In many studies, this neuronal modulation is mediated by astrocyte Ca^{2+}-dependent increases in extracellular adenosine, which binds neuronal purinergic receptors[61,82]. The circuit-level significance of these relationships is illustrated by *in vivo* studies showing that manipulation of astrocyte-specific Ca^{2+} activity, or adenosine signaling, alters sleep- and wake-specific cortical dynamics and tends to promote NREM sleep[37]. However, it remains unclear how endogenous sleep/wake signals, including wake-specific neuromodulators, shape astrocytic regulation of arousal via Ca^{2+} and adenosine signaling.

Since cortical astrocytes express H1R at higher levels than any other monoaminergic or cholinergic neuromodulatory GPCRs[8], we investigated how the wake-specific signal, HA, modulates astrocyte Ca^{2+} and purinergic signaling in the cortex. This investigation builds on noradrenergic studies showing that astrocyte-specific Adra1a regulates cortical synchrony[10] and drives Ca^{2+}-dependent release of adenosine[12,14], and thus aims to contribute to a model in which astrocytes integrate wake-specific neuromodulators via Ca^{2+} to ultimately regulate neuronal activity via adenosine signaling.

In this Chapter, we present *ex vivo* data illustrating how HA modulates astrocyte Ca^{2+} activity and extracellular ATP (the adenosine precursor) dynamics in the visual cortex (V1), a cortical region that contributes to arousal regulation[10,43], and where astrocytes integrate neuromodulatory input[38,83]. Specifically, we demonstrate: 1) the dose-dependency of HA-triggered astrocytic Ca^{2+}

activity, 2) the HA receptor subtype required for Ca^{2+} responses, and 3) the cell-autonomous nature of HA-triggered astrocyte Ca^{2+}. Next, we examine how blockade of HA signaling, both throughout cortex, and specifically in astrocytes, affects ATP release. Finally, I present results that I contributed to a publication by Silvia Pittolo et al. This study showed that astrocytes in medial prefrontal cortex (mPFC) respond to DA via adrenergic receptors. Building on work demonstrating DA stimulated astrocytic ATP release in nucleus accumbens[62], I tested whether DA drives ATP release in mPFC via Adra1a, the receptor that mediates DA-triggered astrocytic Ca^{2+} as shown by Silvia.

Overall, our findings suggest that astrocyte-specific H1R signaling—and likely astrocytic neuromodulatory signaling more broadly—regulates astrocyte Ca^{2+} and extracellular ATP/adenosine, two key determinants of arousal.

2.2 RESULTS

2.2.1 HA triggers dose-dependent Ca^{2+} responses in cortical astrocytes

To determine cortical astrocyte sensitivity to histaminergic signals, we characterized the dose-dependency of their Ca^{2+} responses to HA. We used 2P imaging of an astrocytic Ca^{2+} sensor (GCaMP6f) in adult, acute V1 slices before and after bath-applying a range of HA concentrations. We tested 0.5, 5, and 100 μM HA based on published data showing Bergmann glia respond to 1–100 μM HA with an EC_{50} of 10 μM[84]. Since neurons also express HA receptors, we applied 1 μM TTX in the bath to block neuronal action potentials (Fig. 2.4.1A). We quantified astrocyte Ca^{2+} activity using the event-detection software AQuA[85] (Fig. 2.4.1B).

To capture changes in both Ca^{2+} event rate and area (Fig. 2.4.1C; Fig. 2.4.2), we quantified the change in percent active pixels before and after HA addition (Δ pixels active, Fig. 2.4.1D)[86] and

the area under the Δ pixels active curve (AUC, Fig. 2.4.1D–E). We found that all HA concentrations triggered an increase in Δ pixels active compared to baseline (Fig. 2.4.1D) and observed dose-dependent relationships for both maximum Δ pixels active and AUC (Fig. 2.4.1E). Concentration-dependent differences in these two features (Fig. 2.4.1E) highlight the different temporal response dynamics triggered by each HA concentration. 0.5 μM HA triggered temporally discrete Ca^{2+} events, 5 μM triggered a more sustained increase in Ca^{2+} event number, and 100 μM HA triggered a highly synchronized, relatively brief increase in event number with a concomitant increase in event size and duration (Fig. 2.4.1C–D; Fig. 2.4.2C; Video 1–2). The amplitude, area, and duration of discrete events also changed in a concentration dependent manner (Fig. 2.4.2C). 0.5 μM HA did not affect amplitude or duration and only triggered a small increase in event area, while 5 and 100 μM clearly increased all three event metrics (Fig. 2.4.2C). The spatiotemporally discrete astrocyte Ca^{2+} dynamics observed here in response to 0.5 and 5 μM HA likely reflect physiological astrocyte Ca^{2+} responses to HA, since microdialysis[65,87] and fast-scanning voltammetry data[88,89] suggest that *in vivo* extracellular [HA] is between 1.25 nM–8 μM. Overall, our results demonstrate that cortical astrocytes respond to a wide range of HA concentrations, which fall within the estimated physiological range of extracellular [HA] in the cortex.

2.2.2 HA-triggered astrocyte Ca^{2+} activity is H1R-dependent

Because RNA-sequencing data show that cortical astrocytes express higher levels of H1R relative to other histamine receptors (H2R, H3R)[8,9], we hypothesized that the HA responses we observed would require H1R activation, consistent with G_q-coupling of H1R and with astrocyte Ca^{2+} data from cerebellum[84], hippocampus[90], and olfactory bulb[91]. To test whether H1R mediated HA-triggered cortical astrocyte Ca^{2+}, we 2P-imaged astrocyte GCaMP6f activity while

pharmacologically blocking H1R (Fig. 2.4.3A, 50 μM chlorpheniramine), and bath-applied 50 μM HA, a concentration that triggers robust Ca^{2+} elevations based on our dose-response data (Fig. 2.4.1). Inhibition of H1R completely abolished the HA-triggered astrocyte Ca^{2+} response (Fig. 2.4.3B–D), including HA-triggered increases in Ca^{2+} event amplitude, duration, and area (Fig. 2.4.3E), suggesting that HA-triggered astrocyte Ca^{2+} is mediated by H1R with little-to-no contribution by H2R or H3R.

2.2.3 Astrocyte-specific H1R expression is required for HA-triggered astrocyte Ca^{2+} activity

The pharmacological inhibition of H1Rs above was not cell type-specific. To next test whether the HA-triggered Ca^{2+} activity in astrocytes required astrocyte-specific H1R expression, we compared Ca^{2+} responses to HA in wild-type (WT) and H1R conditional knockout (cKO) astrocytes. Thus, we used neonatal (P0–3) viral injections in $H1R^{fl/fl}$ mice to drive astrocytic Cre and GCaMP6f expression via the GFAP promoter and measured astrocyte Ca^{2+} activity in acute V1 slices from ≥P28 mice (Fig. 2.4.4A–F; Methods). In this experimental strategy, acute V1 slices contained a mosaic of WT and cKO astrocytes, which facilitated within-slice paired comparisons (Fig. 2.4.4A; Fig. 2.4.7A–B). Astrocyte-specific deletion of H1R in V1 was verified by analyzing colocalization of astrocytic Cre-RFP, the astrocyte marker S100β and H1R mRNA in fixed tissue via RNAscope (Fig. 2.4.4E–F). Additionally, since neuronal precursors express GFAP[92,93] and mature neurons express H1R[9], we ensured that neurons were not transduced with the Cre-RFP virus by quantifying overlap of Cre and NeuN expression (percentage of pixels in RFP^+ soma that were $NeuN^+$). On average, 7% of the pixels in individual RFP^+ soma were $NeuN^+$, while 96% of pixels were RFP^+ (Fig. 2.4.4C–D; Fig. 2.4.5B–C). This demonstrates lack of neuronal Cre-RFP

expression, which confirms our observation that RFP^+ cells consistently exhibited astrocytic morphology (Fig. 2.4.4C, E).

We next used 2P imaging to record GCaMP6f dynamics in WT (RFP^-) and cKO (RFP^+) astrocytes before and after 50 μM HA addition, and analyzed AQuA-detected Ca^{2+} activity within manually drawn regions-of-interest (ROIs) around WT and cKO astrocytes (Fig. 2.4.6A; Fig. 2.4.7A–B; Video 3). WT astrocytes exhibited a robust increase in the percent of each ROI active (% ROI active) when stimulated with 50 μM HA. This effect was almost completely abolished in cKO astrocytes (Fig. 2.4.6B–C), which showed a small increase in % ROI active in cKO astrocytes (~20% in WT vs ~2% in cKO cells; Fig. 2.4.7C). This modest change in the % ROI active for cKO cells is likely due to increased event rate, as evidenced by the similar increase in the number of co-occurring Ca^{2+} events in cKO cells compared to WT cells (Fig. 2.4.7E), without a corresponding increase in Ca^{2+} event area (Fig. 2.4.7D). These results suggest that cKO cells are not directly responsive to HA but maintain some HA-triggered activity via connectivity to the rest of the astrocyte network or in response to activation of neuronal HA receptors.

To test whether the cKO astrocytes were unresponsive specifically to HA or more generally, we bath-applied 10 μM NE—which drives large astrocyte Ca^{2+} elevations in cortex[10,39,40,94–96]—immediately after the HA application (Fig. 2.4.6A). The cKO astrocytes showed clear Ca^{2+} increases when NE was bath-applied (Fig. 2.4.6B, D), demonstrating that they retain Ca^{2+} responsiveness and their non-response to HA was specific to this neuromodulator. Neighboring WT astrocytes were almost unresponsive to NE addition after HA stimulation (Fig. 2.4.6B, D). While this may be due to exhaustion of Ca^{2+} stores, since we saw no difference in WT and cKO Ca^{2+} responses to NE when slices were not previously stimulated with HA (Fig. 2.4.6C, F; Video 4), we think it is unlikely because NE responses in cerebellar astrocytes recover within 4 minutes

after a single preceding NE stimulation[84], and HA and NE addition were separated by at least 10 minutes here. Instead, our results could reflect HA-triggered changes in astrocyte activity that outlast acute H1R activation, consistent with the observation that the decrease in NE-triggered WT responses relative to neighboring cKO responses is not correlated with the time between HA and NE addition (Fig. 2.4.6E). Together, these data show that HA directly activates astrocytes via H1R, leading to acute Ca^{2+} elevations in H1R-expressing astrocytes.

2.2.4 HA stimulates delayed ATP release that requires astrocytic H1R activity

Astrocyte Ca^{2+} elevations lead to release of ATP, which is extracellularly metabolized to adenosine, a known sleep promoter released during wakefulness. Thus, we hypothesized that HA might drive astrocytic ATP release. To test this, we employed a similar neonatal viral strategy used earlier (Fig. 2.4.1; Fig 2.4.4) to express a fluorescent extracellularly facing ATP sensor, GRAB-ATP[97], on astrocytes in V1, and then examined how H1R signaling modulates extracellular ATP dynamics. Thus, we used 2P imaging to record GRAB-ATP dynamics in acute V1 slices (Fig. 2.4.8A–C) before and after 50 μM HA addition.

Since the characteristics of extracellular ATP dynamics in acute cortical slices were unknown, we first imaged GRAB-ATP using a 60x objective to capture a broad range of ATP event sizes (Fig. 2.4.8A). Discrete GRAB-ATP events were detected using AQuA (Fig. 2.4.8A) and we found that HA caused a minutes-long delayed increase in ATP events/min relative to baseline (Fig. 2.4.8D, G). ATP events were infrequent, occurring at a maximum rate of 1.2 events per minute, and large enough (post-HA mean = 165 μm^2) to be imaged at a lower magnification, so proceeding experiments were conducted using a 20x objective.

Next, we tested whether the increase in ATP release was dependent on H1R. We therefore imaged GRAB-ATP in WT slices with or without pharmacological blockade of H1R (Fig. 2.4.8B). Separately, we imaged GRAB-ATP in H1R cKO slices (Fig. 2.4.8C). As with the 60x data, we found that HA caused a minutes-long (>10 minutes post-HA) delayed increase in ATP events/min relative to baseline (Fig. 2.4.8E, H). This increase was dependent on H1R, as it was absent in the H1R cKO slices and when we pharmacologically inhibited H1R (Fig. 2.4.8E–F, H–I). Finally, in untreated WT slices post-HA, the median ATP event duration and area was 5 seconds and 63 μm^2, respectively (data not shown). These event metrics align with measurements in a recent study that used GRAB-ATP to record astrocytic ATP release *in vivo* (median duration ~10 seconds, area ~100 μm^2)[60], suggesting that our results reflect physiological astrocyte responses rather than an artifactual response specific to the acute slice preparation.

2.2.5 DA stimulates delayed ATP release in mPFC

In a separate work published by Silvia Pittolo et al.[15], which aimed to understand how DA shapes astrocyte physiology in mPFC, I tested how DA modulates extracellular ATP dynamics via astrocytes. Silvia demonstrated that DA triggers Ca^{2+} elevations in mPFC astrocytes via Adra1a, a receptor thought to stimulate ATP release[11]. We therefore tested whether DA modulates ATP release via Adra1a. To do this, we utilized neonatal virus injections to express GRAB-ATP in mPFC astrocytes. Subsequently, we bath-applied 10 μM DA and used 2P imaging to monitor GRAB-ATP dynamics in acute mPFC slices, with or without pharmacological blockade of Adra1a (Fig. 2.4.9F, K).

First, we showed that GRAB-ATP robustly responds to bath application of 50 μM ATP (Fig. 2.4.9A–E), demonstrating that this sensor worked as expected in acute mPFC slices. Next, we

found that DA, like HA, triggered a delayed increase in ATP release as measured by overall change in GRAB-ATP fluorescence over time (Fig. 2.4.9H), and ATP event rate pre- and post-addition of DA (Fig. 2.4.9I). Addition of an Adra1a antagonist (10 μM Doxazosin) blocked the increase in ATP release (Fig. 2.4.9M–N), demonstrating that DA drives ATP release via activation of Adra1a, the receptor shown to mediate DA-triggered Ca^{2+} elevations in mPFC astrocytes. It should be noted that while DA triggered ATP release as detected by GRAB-ATP expressed on astrocytes, we did not test whether this effect required astrocyte-specific responses to DA. For methods used to collect all data presented in Figure 2.4.9, see Silvia Pittolo et al.[15].

2.3 DISCUSSION

2.3.1 HA directly activates cortical astrocytes via H1R

Astrocytes are poised to propagate neuromodulatory signals across cortex, as they respond to these signals with Ca^{2+} elevations and form continuous, gap junctionally coupled networks that facilitate widespread regulation of neurons[16,35,36,98]. Yet, whether neuromodulators directly activate astrocytes, rather than indirectly via neuronal activation, remains an under-explored area. I showed here that HA drives dose-dependent Ca^{2+} activity in cortical astrocytes via astrocyte-specific H1R, adding HA—alongside NE[10,12,52] and DA[62]—to the list of neuromodulators that directly activate astrocytes to sense and regulate neuronal activity. Further astrocyte-specific KO studies will help round out the still incomplete picture of which neuromodulatory inputs astrocytes are specifically tuned to, and how these inputs distinctly regulate astrocyte function.

One clue to how neuromodulatory inputs may differentially affect astrocyte activity are the specific spatiotemporal patterns of Ca^{2+} triggered by different neuromodulators. Here, H1R-dependent Ca^{2+} elevations were largely confined to individual astrocytes (Video 3), with limited

intercellular propagation, indicating a spatially localized response. However, we did observe increased Ca^{2+} event synchrony in both WT and H1R cKO astrocytes after HA application, suggesting that gap junctions, or intercellular signals like ATP release, may communicate H1R signals across among cells. Through this kind of mechanism, focal HA release from histaminergic axons *in vivo* could cause spatially confined Ca^{2+} elevations in H1R expressing astrocytes, while also driving a network-wide increase in astrocyte Ca^{2+} event synchrony. These spatially distinct modes of astrocyte Ca^{2+} could facilitate both local astrocytic regulation of synaptic activity near HA release sites and broader regulation of circuit activity.

We also showed that HA stimulation of Ca^{2+} release led to strong attenuation of NE-triggered Ca^{2+} responses even many minutes after initial HA stimulation (Fig. 2.4.6B, D). Since Ca^{2+} stores replenish within minutes of IP3-mediated Ca^{2+} release[99], this effect may indicate that H1R activation shapes astrocyte Ca^{2+} responses to non-histaminergic inputs, consistent with recent work showing that a single neuromodulator gates astrocyte responses to other neuromodulators[100] and underscoring the potential synergistic effects of distinct neuromodulators on astrocyte physiology.

2.3.2 Neuromodulators trigger ATP release in cortex

Having demonstrated cell-autonomous, HA-triggered Ca^{2+} responses in astrocytes, we were interested in uncovering H1R-dependent astrocyte outputs downstream of Ca^{2+}. Since others had shown that GPCR mediated astrocyte Ca^{2+} leads to ATP/adenosine mediated neuronal modulation[82], we tested how HA regulates extracellular ATP dynamics in V1, and in a separate project, we examined DA regulation of ATP dynamics in mPFC. Both neuromodulators

stimulated relatively delayed ATP release in cortex, and in the case of HA, this was dependent upon astrocyte-specific H1R.

Several questions remain regarding how neuromodulators regulate astrocytic ATP release. In particular, the molecular mechanism underlying ATP dynamics described here is unknown. Possibilities include Ca^{2+}-dependent changes in exocytosis, transport, or metabolism of ATP/adenosine[61]. The focal nature of GRAB-ATP events (Fig. 2.4.8B and 2.4.9G) and the delayed increase in ATP event rate (Fig. 2.4.8E and 2.4.9H) that we observe are consistent with the hypothesis that neuromodulator-triggered astrocyte Ca^{2+} drives increased *exocytosis* of ATP, potentially via lysosomal pathways, as suggested by several studies. Most compelling, a recent *in vivo* study using GRAB-ATP demonstrated that stimulation of astrocytic G_q signaling triggers VNUT-dependent ATP release, peaking 5–10 minutes after initial G_q-mediated Ca^{2+} elevations[60]. Similar minutes-long delays between Ca^{2+} elevations and ATP release have been reported in cell culture [80,81] and hippocampal slice[81] studies, which highlight lysosomal exocytosis as the primary mechanism of astrocytic ATP release. Thus, solid scientific precedent motivates investigation into the hypothesis that neuromodulators trigger ATP release specifically via Ca^{2+}-dependent lysosomal exocytosis in astrocytes.

Ca^{2+}-dependent ATP release has been observed across diverse experimental preparations–cell culture, brain slices, and *in vivo*–suggesting that the ATP release we observed is not an artifact of acute slice preparation, a reasonable concern considering ATP release increases in brain injury models[97]. Instead, our results likely reflect normal physiological astrocytic ATP responses to neuromodulators in the cortex. To confirm this, future *in vivo* studies employing 2P-imaging strategies, such as those used by Li et al. (2024), are warranted. Future experiments should also extend our findings by investigating the combined effects of multiple neuromodulators, such as

HA, DA, and NE, on ATP dynamics. Such combinations may evoke Ca^{2+} elevations sufficient to drive more robust ATP exocytosis than individual neuromodulators, potentially contributing to extracellular adenosine accumulation during wakefulness and subsequent adenosine mediated neuronal modulation. Experiments combining GRAB-ATP/Ado imaging with electrophysiology in acute cortical slices could test this hypothesis. For example, neuromodulator-triggered changes in purinergic circuit modulation could be examined before and after astrocyte-specific deletion of neuromodulatory GPCRs or lysosomal machinery.

To summarize, we have shown that DA triggers ATP release over astrocytic territories in the mPFC, while HA drives ATP release in V1 via H1R activation in astrocytes. Although the underlying cellular signaling pathways remain to be elucidated, these findings align with studies showing that astrocyte-specific neuromodulatory GPCRs, including DA D1 receptors in a subcortical brain region [62] and Adra1a in the mammalian [12] and fish brain [14], trigger ATP release that shapes neuronal dynamics. Thus, our findings bolster a growing body of evidence identifying the integration of neuromodulators to drive purinergic modulation of neuronal activity as a core astrocytic function evolutionarily conserved across multiple species and diverse brain regions.

2.4 FIGURES

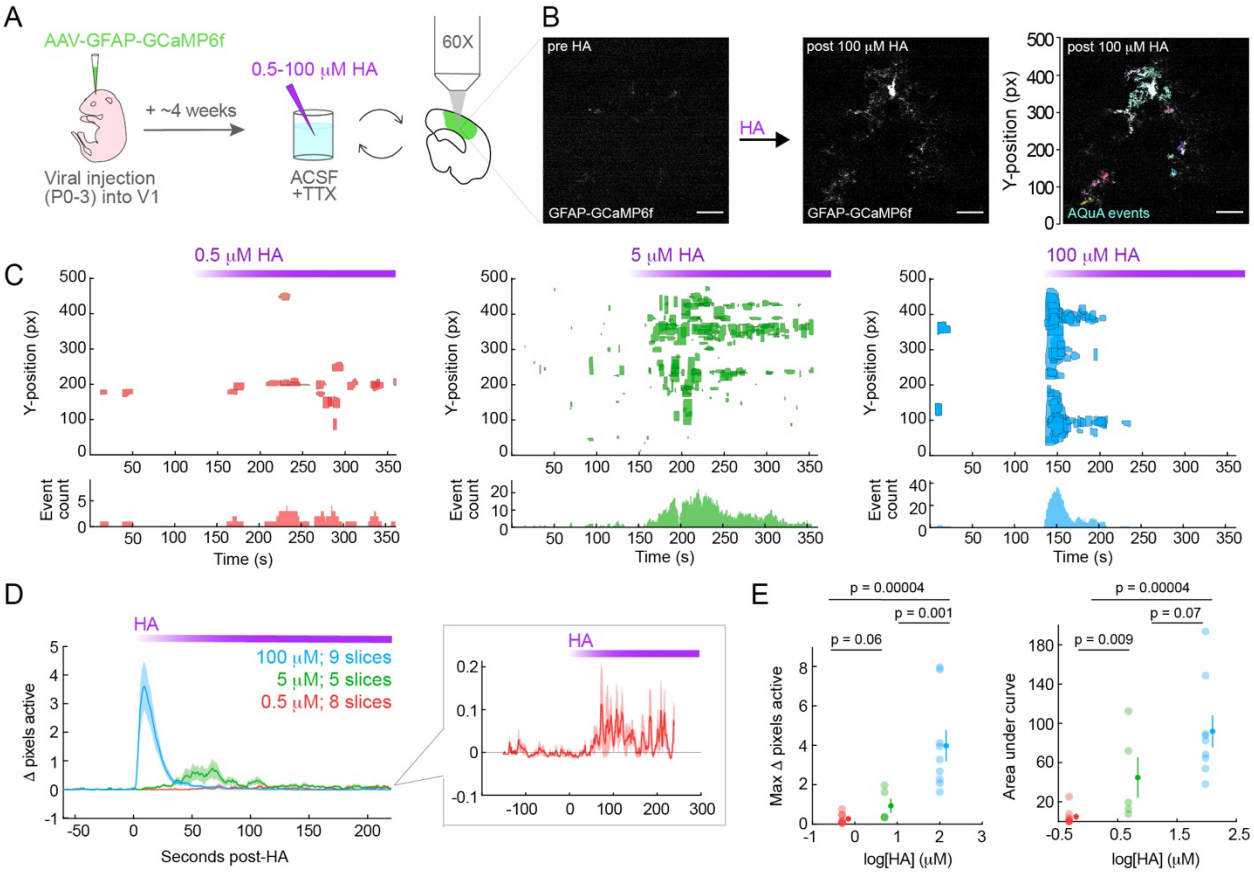

Figure 2.4.1. HA drives dose-dependent Ca^{2+} responses in cortical astrocytes.
A) Experimental schematic. Neonatal virus injection induces GCaMP6f expression in cortical astrocytes. After > 4 weeks, acute V1 slices are 2P-imaged before and after bath-application of 0.5, 5, or 100 μM HA. 1μM TTX is in bath to block action potentials for the entirety of experiments. **(B)** Four summed frames of 2P time-series show representative GCaMP6f fluorescence before (left) and after (middle) 100 μM HA addition. Right: GCaMP6f fluorescence post-HA with overlaid AQuA-detected events and y-position within FOV. Scale bars = 25 μm. **(C)** Y-axis position and duration of Ca^{2+} events before and after addition of 0.5 (left, red), 5 (middle, green), or 100 (right, blue) μM HA. Lower bar plots show number of active events per second. Purple bar = HA recirculating in ACSF, for C and D. **(D)** Change in % active pixels relative to mean 60s pre-HA. Traces = mean across slices. Shaded error bars = standard error of mean (SEM). Inset = activity triggered by 0.5 μM HA. **(E)** Summary of data in D. Left: maximum Δ pixels active for each slice during 2-min post-HA. Mean ± SEM = 0.5 μM: 0.3 ± 0.1, 5 μM: 0.9 ± 0.4, 100 μM: 4.0 ± 0.8.
(Figure caption continued on the next page.)

(Figure caption continued from the previous page.)
Right: area under the curve (AUC) for each slice during 2-min post-HA. Mean ± SEM = 0.5 μM: 4.8 ± 3.0, 5 μM: 44.7 ± 20.5, 100 μM: 91.8 ± 16.4. p-values calculated via one-sided Wilcoxon rank-sum test.

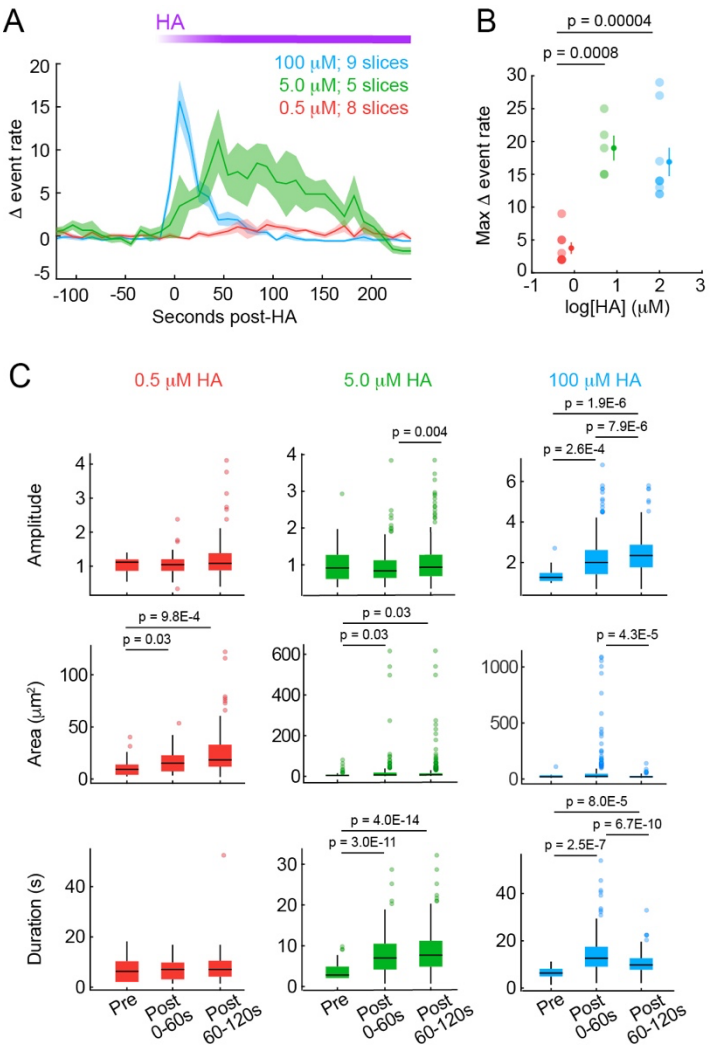

Figure 2.4.2. Dose-dependence of HA-triggered Ca^{2+} event rate and area.
(A) HA-triggered increases in Ca^{2+} event rate (10-s time bins) for 0.5, 5, and 100 μM HA, indicated by red, green, and blue traces, respectively. Each trace is change in event rate relative to mean 60s pre-HA. Shaded error bars = SEM. Purple bar = HA time in recirculating ACSF. **(B)** Summary of data in A. Maximum change in event rate during 2 min post-HA for each slice, with mean ± SEM at right. p-values via one-sided Wilcoxon rank-sum test. **(C)** Distribution of event amplitude, area, and duration in 60-s time bins pre- and post-HA addition for 0.5, 5, and 100 μM HA. p-values via one-sided Wilcoxon rank-sum test.

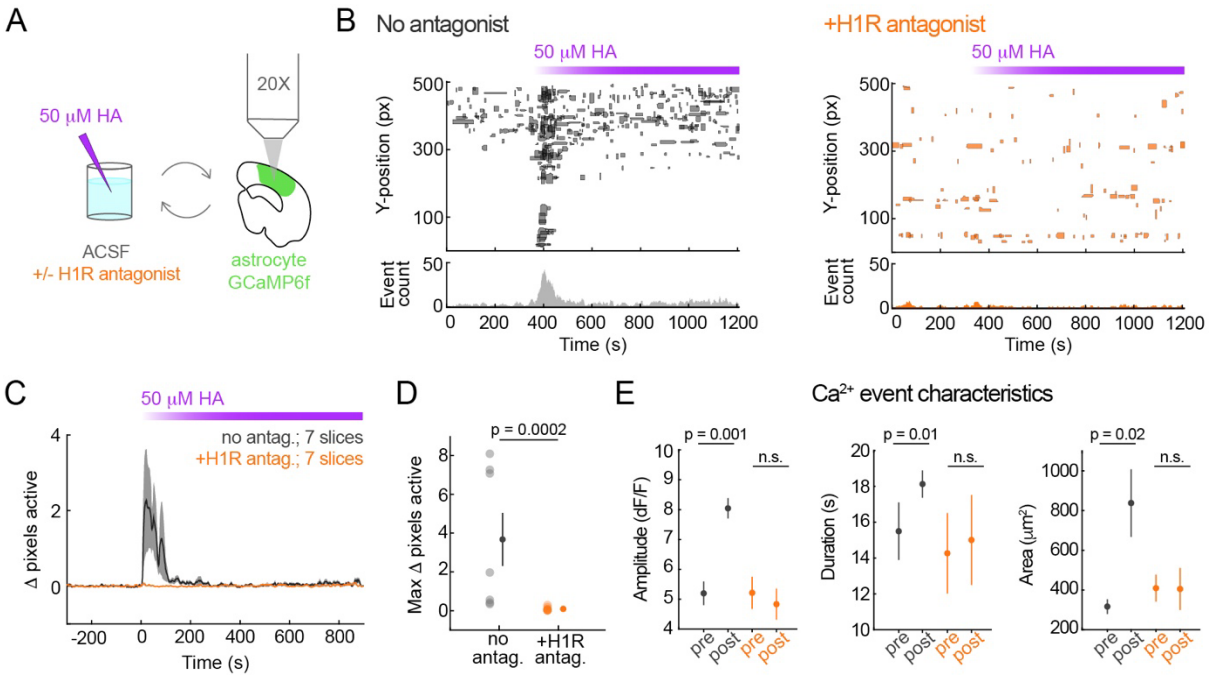

Figure 2.4.3. HA-triggered astrocyte Ca^{2+} is H1R-dependent.
(A) Experimental schematic. Acute V1 slices from adult mice (≥P28) expressing cortical astrocytic GCaMP6f are 2P-imaged before and after 50 μM HA addition (purple). **(B)** Location and duration of Ca^{2+} events before and after 50 μM HA addition without (left, grey) or with 50 μM H1R antagonist chlorpheniramine (right, orange); lower bar plots show number of active events per second. Purple bar = time HA is recirculating. **(C)** Change in % active pixels relative to mean 60s pre-HA ± H1R antagonist. Traces = mean across slices. Shaded error bars = SEM. **(D)** Summary of data in C. Maximum change in active pixels during 2-min post-HA for each slice, with mean ± SEM at right (no antagonist: 3.7 ± 1.4, +H1R antagonist: 0.09 ± 0.04). p-values via one-sided Wilcoxon rank-sum test. **(E)** Amplitude (left), duration (middle), and area (right) of Ca^{2+} events pre- and post-HA ± H1R antagonist. Mean ± 95% CI estimated via bootstrapping with replacement. p-values via permutation test on data before bootstrapping.

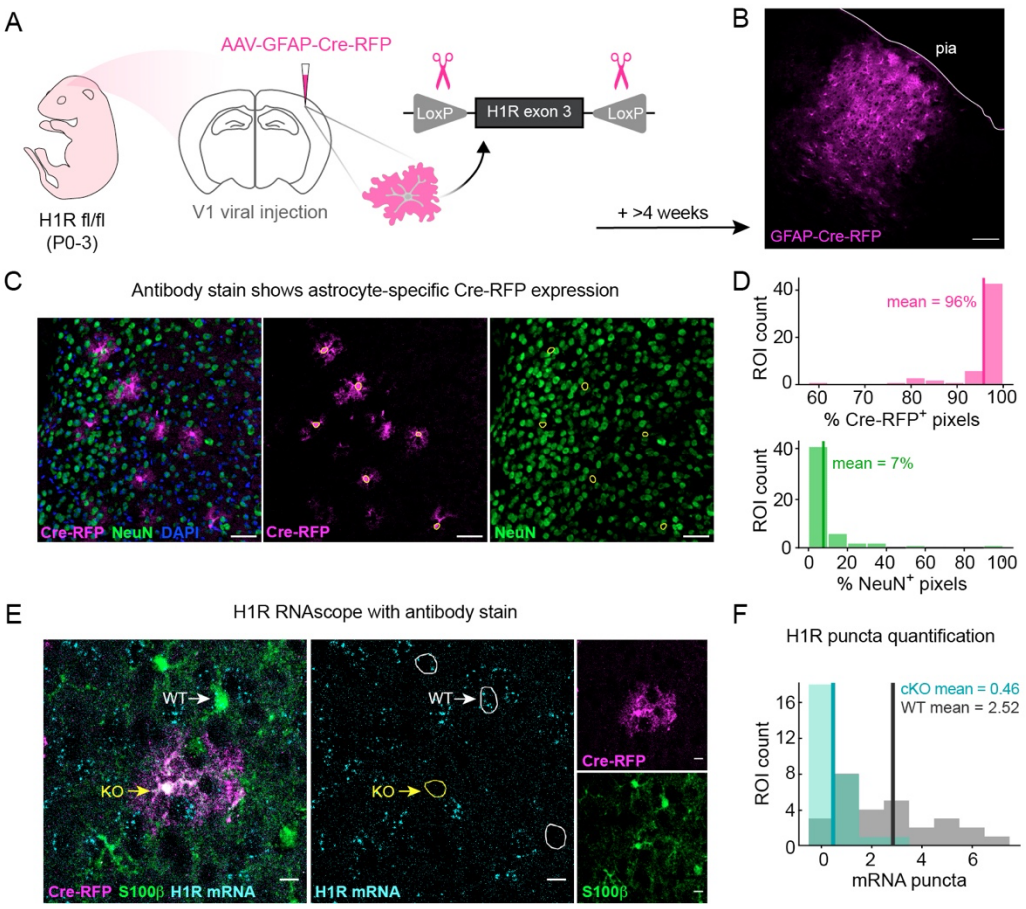

Figure 2.4.4. Astrocyte-specific Cre-virus drives H1R deletion in cortical astrocytes. **(A)** Schematic illustrates H1R conditional knockout procedure. Astrocytic Cre-RFP expression is driven via neonatal virus injections. Cre-mediated recombination excises exon 3, which encodes H1R. Proceeding experiments are conducted after 4 weeks of viral transduction. **(B)** Example confocal micrograph shows localized Cre-RFP expression in the cortex ~4 weeks after neonatal virus injection. Cre-RFP$^+$ cells are morphologically consistent with astrocytes. White line shows pia; scale bar = 100 µm. **(C)** Example confocal micrograph showing astrocytic Cre-RFP (magenta), neuronal NeuN (green), and nuclear marker DAPI (blue). Left: summed z-projection of all three confocal channels. Middle: astrocytic Cre-RFP signal with astrocyte soma ROIs overlaid. Right: NeuN signal with astrocyte soma ROIs overlaid. Scale bars = 50 µm. **(D)** Quantification of Cre-RFP expression in cortical neurons. Histograms show percentage of astrocyte soma pixels that are RFP$^+$ (top, pink) and NeuN$^+$ (bottom, green). Mean percentage of soma pixels that are RFP$^+$ and NeuN$^+$ is 96% and 7%, respectively (n = 57 soma from 6 sections, N = 3 mice). **(E)** Example confocal micrograph showing astrocyte expression of S100β (green), Cre-RFP (magenta), and H1R mRNA (cyan). Left: summed z-projection of all three confocal channels. Middle: RNAscope detected H1R mRNA with white and yellow arrows indicating example WT (S100β$^+$/RFP$^-$/H1R$^+$) and cKO (RFP$^+$/H1R$^-$) soma ROIs, respectively. Right: Cre-RFP expression (top, magenta) and S100β expression (bottom, green). Scale bars = 10 µm. (Figure caption continued on the previous page.)

(Figure caption continued from the previous page.)
(F) Quantification of RNAscope detected H1R mRNA puncta in RFP+ and S100β^{+}/RFP^{-} astrocytes in H1R$^{fl/fl}$ cortex. Histogram shows distribution of 28 cKO soma and 28 randomly sampled data points from a total of 96 WT soma. cKO soma (RFP^{+}; n = 28 soma from 10 sections; N = 3 mice) had a mean of 0.46 puncta and a 36% probability of >0 H1R puncta. WT soma (S100β^{+}/RFP^{-}; n = 28 soma from 10 sections; N = 3 mice) had a mean of 2.52 puncta and a 77% probability of >0 H1R puncta.

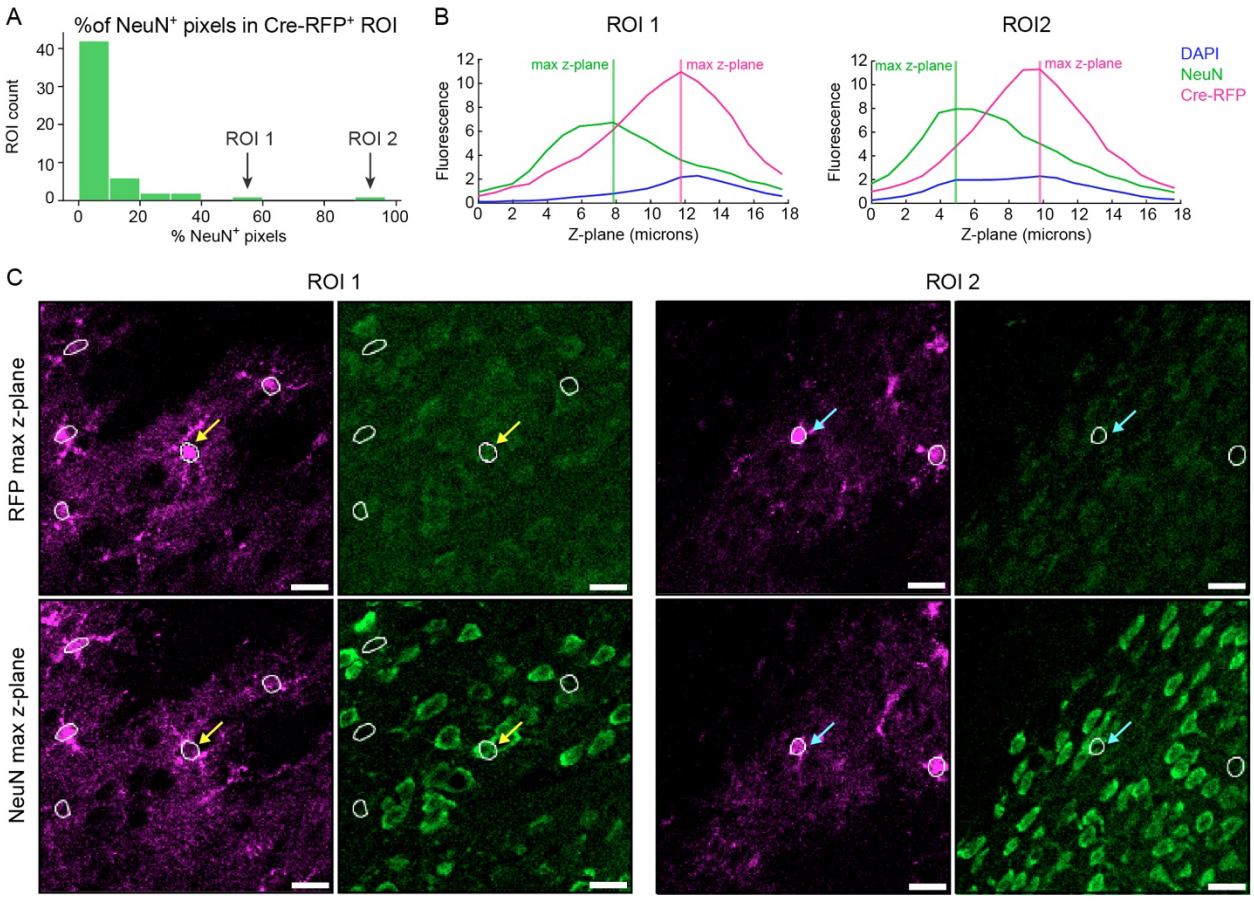

Figure 2.4.5. Two somatic ROIs that exhibit substantial Cre-RFP and NeuN overlap exhibit RFP$^+$ and NeuN$^+$ pixels in distinct z-planes.
(A) Percentage of Cre-RFP$^+$ astrocyte soma pixels that are NeuN$^+$. Arrows point to two cells with >50% RFP and NeuN overlap, which was quantified by generating summed z-projection of NeuN channel, binarizing the z-projection, and then calculating the % of NeuN$^+$ pixels in somatic ROIs. **(B)** Traces show fluorescence level of DAPI (blue), NeuN (green), RFP (pink) across all z-planes in z-stack for ROI 1 (left) and ROI 2 (right) indicated in panel A. Vertical lines show z-plane of maximum fluorescence for NeuN (green) and RFP (pink), revealing no overlap. **(C)** Confocal micrographs show RFP and NeuN fluorescence in ROI 1 indicated by yellow arrows (left four images) and ROI 2 indicated by cyan arrows (right four images). Top row: RFP fluorescence and lack of NeuN fluorescence in z-plane displaying maximum RFP fluorescence for both ROI 1 (left two images) and 2 (right two images). Bottom row: RFP and NeuN fluorescence in z-plane displaying maximum NeuN fluorescence. ROI 1 displays absence of RFP in this plane. ROI 2 exhibits reduced RFP levels and captures the edges of multiple NeuN$^+$ cells rather than an RFP$^+$ individual neuron. Scale bars = 20 μm.

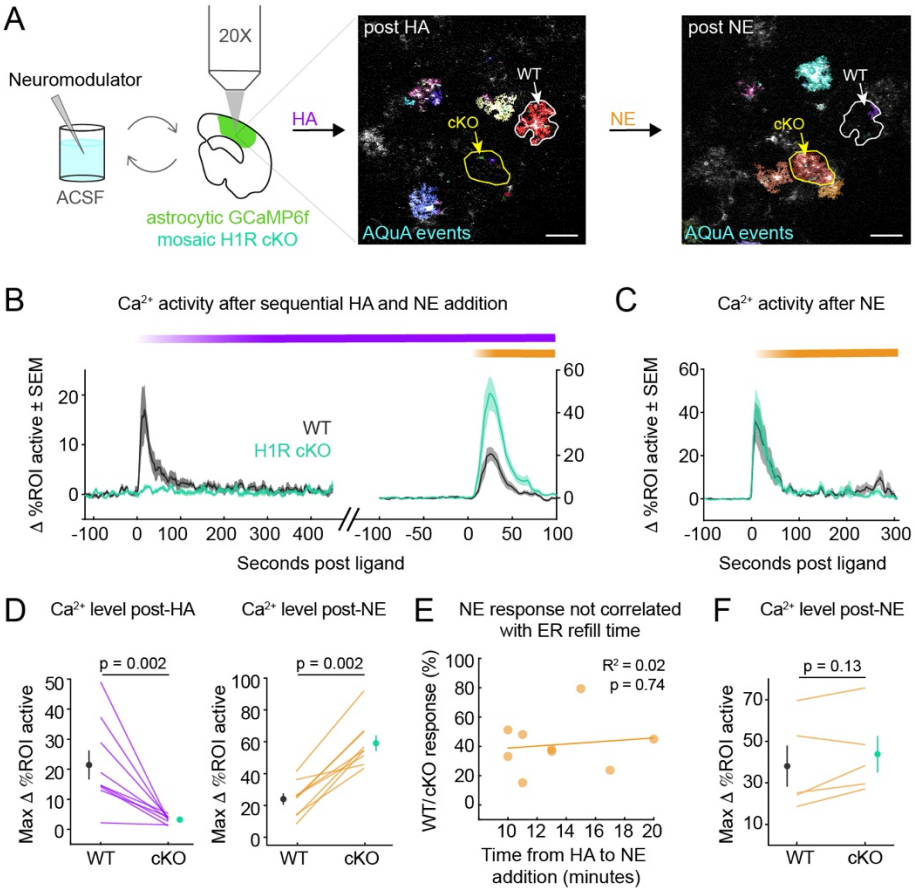

Figure 2.4.6. HA drives astrocyte Ca^{2+} via astrocyte-specific H1R.
(A) Experimental schematic. Acute V1 slices from $H1R^{fl/fl}$ mice expressing astrocytic GCaMP6f ± Cre-RFP are 2P-imaged before and after neuromodulator addition. Example images: four summed frames of 2P time-series with overlaid AQuA events after 50 µM HA (left) and 10 µM NE (right) addition. ROIs and arrows indicate example H1R cKO (yellow arrow) and WT (white arrow) astrocytes (see Methods for identification). Scale bar = 50 µm. **(B)** Mean change in percent of WT or cKO pixels active post-ligand. Purple bar = 50 µM HA addition; orange bar = 10 µM NE addition. Shaded error bars = SEM. **(C)** Mean absolute change in percent of WT or cKO pixels active after 10 µM NE addition (orange bar) to untreated slices. Shaded error bars = SEM. **(D)** Summary of data in B. Left: WT versus cKO mean maximum change in percent-ROI-active post-HA for each slice. Mean across slices ± SEM (WT: 21.4 ± 4.8%; cKO: 3.2 ± 0.4%). Right: post-NE condition (WT: 24.0 ± 3.6%; cKO: 59.1 ± 5.0%). For D and F, p-values calculated via one-sided, paired Wilcoxon rank-sum. **(E)** Linear regression analysis showing correlation between WT/cKO NE-response ratio and the amount of time separating HA and NE addition to recirculating ACSF bath. Each data point shows mean WT/cKO response ratio per slice. Displayed R^2- and p-values indicate no correlation. **(F)** Summary of data in D. Mean maximum change in percent-ROI-active post-NE for each slice. Mean across slices ± SEM (WT: 38.0 ± 9.9; cKO: 43.8 ± 8.8).

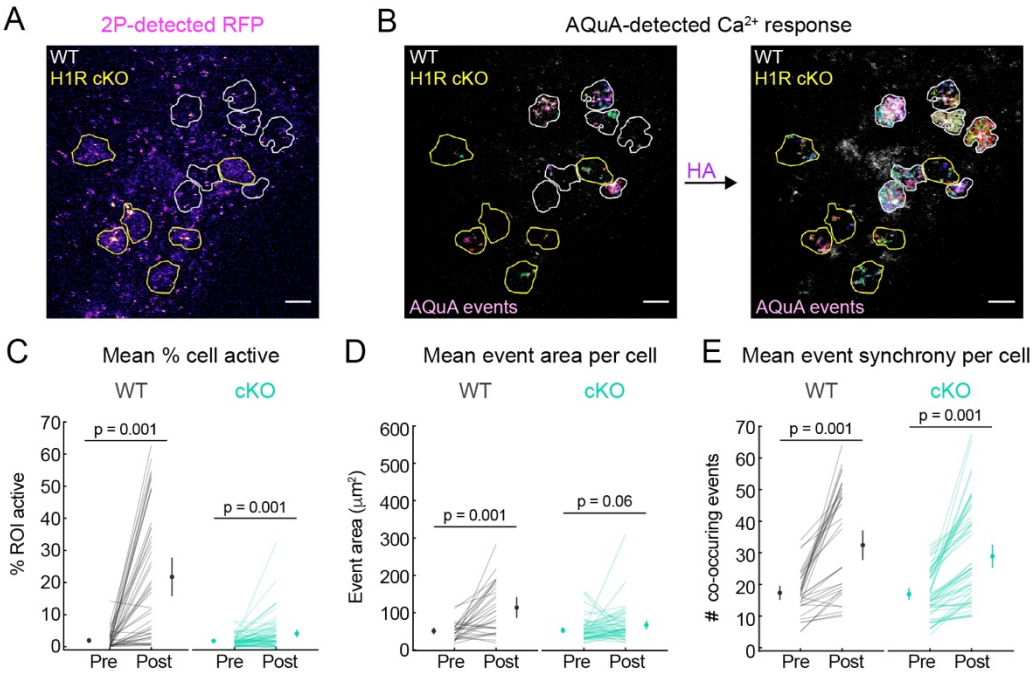

Figure 2.4.7. H1R deletion in astrocytes leads to reduced cell area subsumed by HA-triggered Ca^{2+} while leaving WT levels of event synchrony intact.
(A) Example z-projection of H1R cKO astrocytes identified via live 2P RFP imaging. H1R cKO astrocytes outlined in yellow. WT astrocytes were identified based on GCaMP6f expression (not shown) and are outlined in white. Scale bar = 50 μm. **(B)** Sample z-projection of 2P image showing pre- and post-HA AQuA events. WT ROIs are filled by AQuA events post-HA, while cKO ROIs exhibit increased number of discrete AQuA events relative to pre-HA. Pre- and post-HA z-projections include same number of frames. Scale bars = 50 μm. **(C)** Mean percent-ROI-active during 1 minute pre-HA and 2 minutes immediately following HA. WT ROIs exhibit increased activity (post – pre = 19.9%). cKO cells show a small increase (post – pre = 2.3%). For C–E, data shown are mean ± 95% CI. **(D)** Ca^{2+} event area per cell during 1 minute pre-HA and 30s immediately following HA. WT astrocytes exhibit larger Ca^{2+} events (post – pre = 59.7 μm^2) post-HA, while cKO event area shows no change. Post-HA window is 30s because area increase is short-lived. No difference was detected for cKO ROIs with 30, 60, or 120s window sizes (60 and 120s window data not shown). **(E)** Co-occurring events per cell during 1 minute pre-HA and 2 minutes post-HA. WT and cKO astrocytes exhibit similar increase in co-occurring events (WT post – pre = 15.1 events; cKO post – pre = 12.1 events). For C–E, means and 95% CI are estimated via bootstrapping with replacement; p-values are calculated via permutation test on data before bootstrapping.

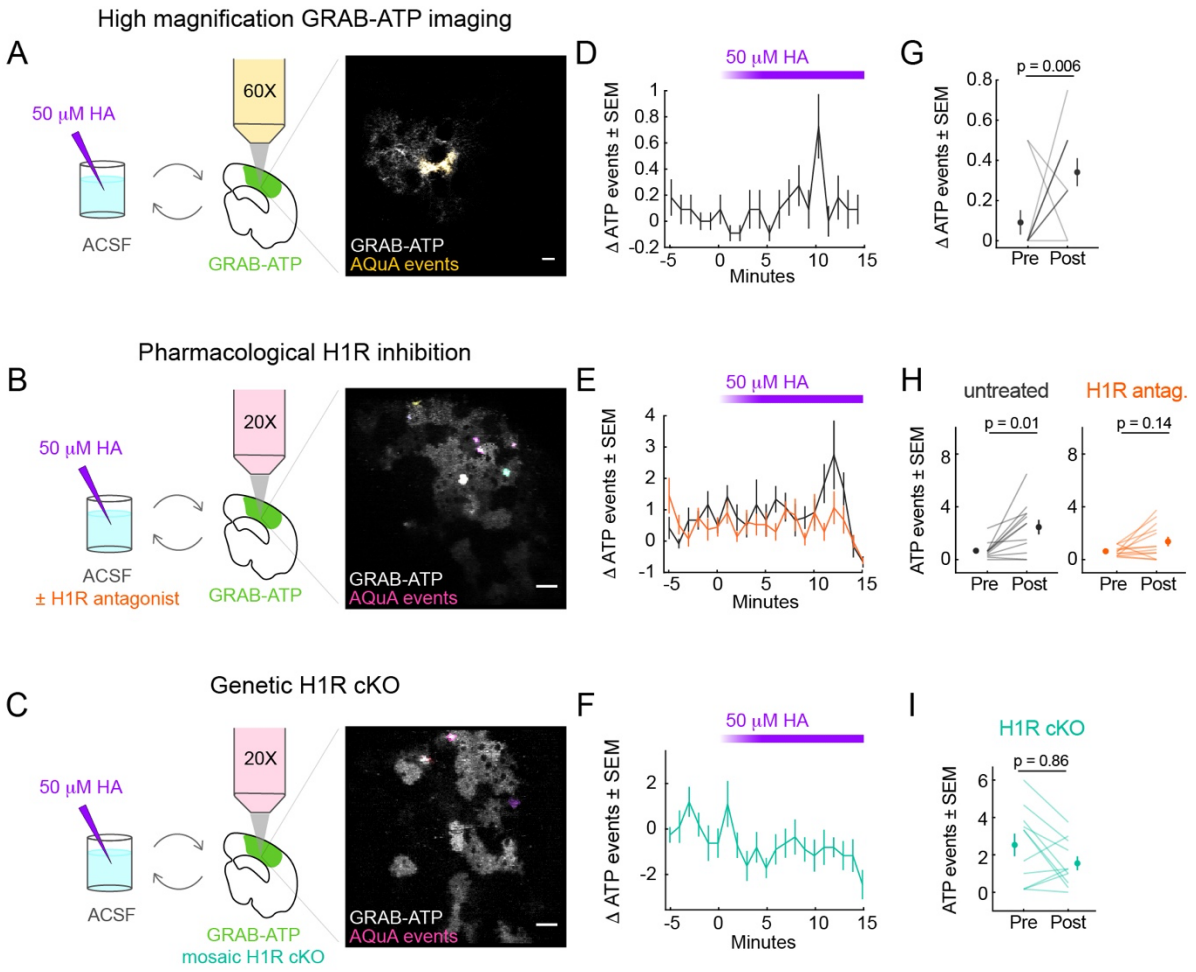

Figure 2.4.8. HA triggers a delayed increase in extracellular ATP events that requires astrocytic H1R activity.
(A-B) Schematics illustrate three *ex vivo* experiments for testing HA modulation of extracellular ATP dynamics. A shows 2P imaging of GRAB-ATP pre- and post-HA at 60x magnification, B shows same experimental set up at 20x ± pharmacological blockade of H1R, C shows same experimental set up, however H1R is mosaically knocked out in astrocytes. Accompanying micrographs show GRAB-ATP fluorescence post-HA with AQuA detected events overlaid. Scale bar for 60x image = 10 μm, scale bar for 20x images = 50 μm. **(D-F)** Change in ATP events/min relative to baseline mean. Binned data shows mean across slices. Error bars = SEM. Purple bar = 50 μM HA addition. D shows data for experiment in A (10 slices). E shows data for experiment in B with no antagonist trace in grey and +H1R antagonist trace in orange (12 slices for no antagonist; 13 slices for +H1R antagonist). Plot in F shows data for experiment in C (11 slices). **(G-I)** Summary data for results shown in panels D–F. Each plot shows mean Δ ATP events/min during 4 minutes before HA addition (pre-HA) and during minutes 10-13 (post-HA). p-values displayed calculated via Wilcoxon rank-sum testing post-HA > pre-HA. G–I summarizes D–F, respectively. For I, Wilcoxon rank-sum calculated p-value for pre-HA > post-HA = 0.15.

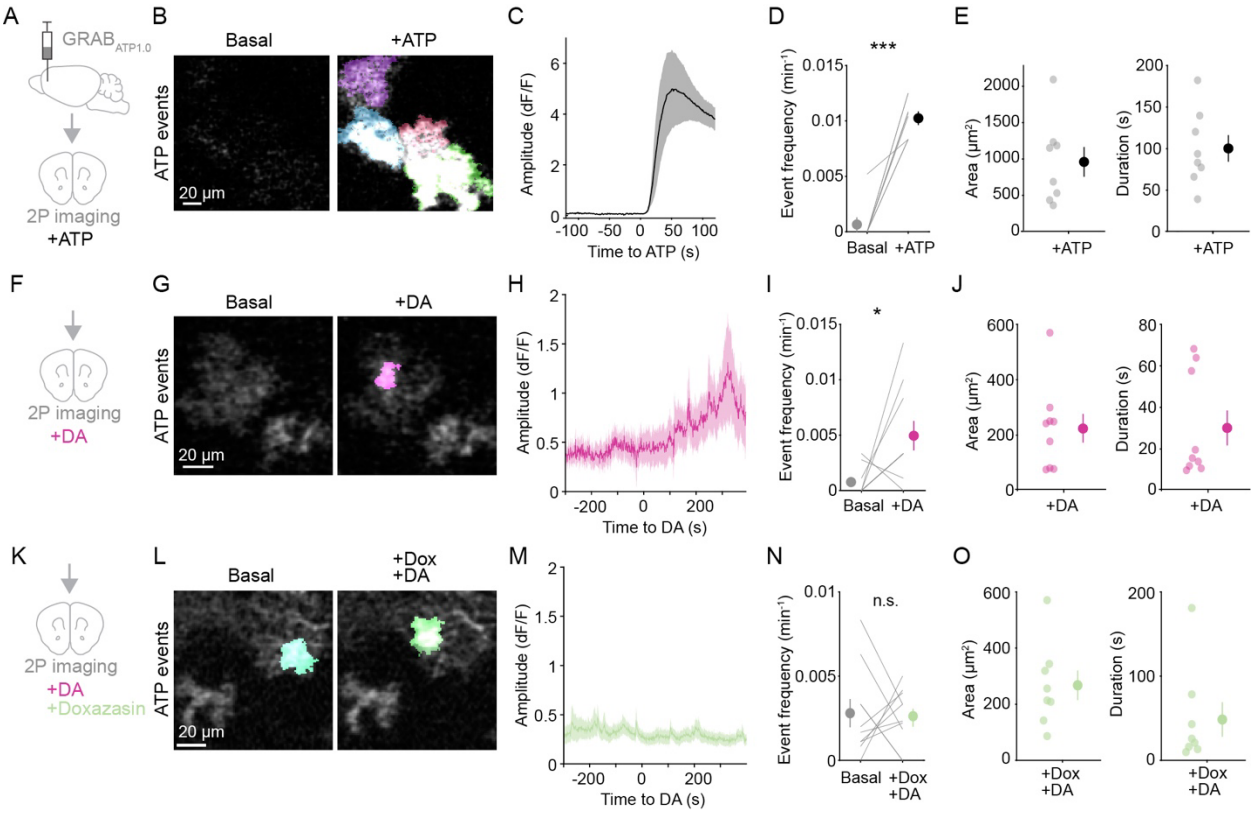

Figure 2.4.9. DA mobilizes ATP at discrete locations at PFC astrocytes via Adra1a.
(A) Schematic for 2P astrocytic $GRAB_{ATP}$ imaging in acute PFC slices. **(B–C)** Continuous bath-application of ATP (50 µM) induces strong, sustained fluorescent signals in astrocytes, shown as (B) PFC astrocytes expressing $GRAB_{ATP}$ (grayscale) with color overlay of AQuA-detected ATP events before (left, basal) and after ATP (right), and (C) time course of the dF/F amplitude of AQuA-detected ATP events relative to exogenous ATP application (t=0). Mean ± SEM of slice traces n=52/62 active/total cells, 8 slices, 3 mice. **(D)** $GRAB_{ATP}$ event rate increases following ATP stimulation. Slice averages (lines) and mean ± SEM (dots and error bars): 0.0007 ± 0.0007 (Basal), 0.010 ± 0.001 (+ATP) min^{-1}. Paired t-test after Anderson-Darling test; ***, $p<10^{-4}$; n=8 slices, 3 mice. **(E)** $GRAB_{ATP}$ events in response to continuous ATP application covered the entire astrocyte territory (left, 1044 ± 224 μm^2) and were sustained (right, 100 ± 16s). Slice averages of active cells (transparent dots) and overall mean ± SEM (solid dots and error bars); n=8 slices, 3 mice. **(F–H)** Application of DA (10 µM) (F) induces localized ATP events, shown as (G) $GRAB_{ATP}$ micrographs and AQuA overlay, which are delayed (H) relative to DA application (t=0). Mean ± SEM of slice averages n=23/101 active/total cells, 10 slices, 5 mice. **(I)** ATP event rate after DA application was higher than baseline. Slice averages (lines) and mean ± SEM (dots and error bars): 0.0007 ± 0.0004 (Basal), 0.005 ± 0.001 (+DA) min^{-1}. Paired t-test after Anderson-Darling test; *, p=0.025; n=10 slices, 5 mice. **(J)** $GRAB_{ATP}$ events in response to DA were smaller than entire astrocyte territories (221 ± 52 μm^2) and time-restricted (30 ± 8s). Slice averages of active cells (transparent dots) and overall mean ± SEM (solid dots and error bars); n=9 slices, 5 mice.
(Figure caption continued on the next page.)

(Figure caption continued from the next page.)
(K–M) In presence of Adra1a antagonist Doxazosin (10 μM), DA (K) does not induce ATP events, as shown by (L) $GRAB_{ATP}$ micrographs and AQuA overlay, and (M) time-course of $GRAB_{ATP}$ event dF/F relative to DA application (t=0, 10 μM). Mean ± SEM of slice averages (line and shaded area). n=41/160 active/total cells, 10 slices, 5 mice. **(N)** In presence of Doxazosin, DA application does not increase ATP event rate. Slice averages (lines) and mean ± SEM (dots and error bars): 0.0028 ± 0.0008 (Basal), 0.0026 ± 0.0005 (+Dox/+DA) min^{-1}. Paired t-test after Anderson-Darling test; n.s., p=0.878; n=10 slices, 5 mice. **(O)** $GRAB_{ATP}$ events in presence of Doxazosin are similar in size (267 ± 53 μm^2) and duration (48 ± 20s) to those observed in DA alone. Slice averages of active cells (transparent dots) and overall mean ± SEM (solid dots and error bars); n=10 slices, 5 mice.

Figure 2.4.9 with legend is published: Pittolo S, Yokoyama S, Willoughby DD, Taylor CR, Reitman ME, Tse V, Wu Z, Etchenique R, Li Y, Poskanzer KE. Dopamine activates astrocytes in prefrontal cortex via α1-adrenergic receptors. Cell Rep. 2022 Sep 27;40(13):111426. doi: 10.1016/j.celrep.2022.111426. PMID: 36170823; PMCID: PMC9555850.

2.5 METHODS

2.5.1 Animals

All animal protocols in this study were approved by the University of California, San Francisco Institutional Animal Care and Use Committee (IACUC). Mice were provided food and water a*d libitum* while being housed on 12:12 light-dark cycle. Transgenic floxed-H1R mice ($H1R^{fl/fl}$) were generated by GemPharmatech (strain number T007142) using the CRISPR/Cas9 system to insert loxP sites flanking exon 3, which contains most of the H1R coding region. *In vivo* experiments were carried out in adult wild-type C57BL/6J mice and transgenic $H1R^{fl/fl}$ mice at 8–12 weeks old. *Ex vivo* experiments were done in P28–58 Swiss, C57BL6, or $H1R^{fl/fl}$ mice. Male and female mice were used in experiments as available. All sleep recordings for fiber photometry and electrophysiology experiments were performed during the light cycle.

2.5.2 Surgical procedures

Fluorescent indicators GCaMP6f, jRGECO, and GRAB-ATP1.0 were virally expressed via neonatal, intracortical virus injections. Pups (P0–3) were anesthetized on ice for 3 min. A glass needle with ~5 μm diameter tip was loaded with 2 μl of either *AAV5-GfaABC1D-cyto-GCaMP6f-SV40* (1.9E13 vg/mL), *AAV9-pGp-AAV-gfa(abc1d)-jRGECO1b* (3.19E13 vg/mL), or *AAV9-GfaABC1D-ATP1.0* (1.78E13 vg/mL) and 0.5 μl of Fast Green dye. After positioning pups on a digital stereotax, coordinates were zeroed at lambda. Virus was then injected at four injection sites in a 2 × 2 square grid. The first injection site was 0.8–0.9 mm lateral and 1.5–1.6 mm rostral from lambda and all four injection sites were 0.8 mm apart. Using a microsyringe pump (UMP-3, World Precision Instruments), 30–80 nl of virus was injected at two depths (0.1 and 0.2 mm below the skull) at each injection site at 3 nl/s. After recovery from anesthesia, all injected pups were returned

to their home cage. For H1R cKO experiments, transgenic $H1R^{fl/fl}$ pups were injected with 60–80 nl of *AAV5-GFAP(0.7)-RFP-T2A-iCre* (5.0E12 vg/mL) at a 1:1 ratio with either *AAV5-GfaABC1D-cyto-GCaMP6f-SV40,* or *AAV9-GfaABC1D-ATP1.0*, depending on the experiment. The same procedure was used for experiments using *AAV9-pGp-AAV-gfa(abc1d)-jRGECO1b* to measure astrocyte Ca^{2+}, however *AAV5-GFAP(0.7)-EGFP-T2A-iCre* (2.69E13 vg/mL) was used instead of the RFP-tagged Cre virus.

2.5.3 Two-photon imaging

Coronal, acute V1 slices (300-μm thick) were collected from mice P28–58. For acute slice preparation, mice were decapitated according to an IACUC-approved protocol and the brain was dissected while submerged in ice-cold sucrose solution. Slices were cut in ice-cold sucrose solution using a vibratome (VT 1200, Leica) and immediately transferred to room temperature (RT), continuously aerated (95% O_2/5% CO_2) standard artificial cerebrospinal fluid (ACSF). After collection, all slices were incubated in a 37°C water bath for 30 minutes and then kept at RT for imaging. For bath application experiments, each slice was allowed to rest for at least 5 minutes in the recording chamber with recirculating ACSF and 1 μM TTX to block neuronal action potentials. An imaging plane, at an average slice depth of 42.96 ± 13.83 μm, was selected based on reporter expression density and astrocyte health. Images were acquired using a custom-built 2P microscope that included an upright fluorescence microscope and the basic components for 2P imaging: one Ti:Sa laser (MaiTai, SpectraPhysics), Pockel cell (Conoptics) for modulating laser power, linear galvanometer (Cambridge Technology) for laser scanning, emission filters, photomultiplier tubes (Hamamatsu), and ScanImage software (version SI5.7) for image acquisition. Laser power was set

such that astrocyte somas were visible, but laser-induced astrocyte GCaMP6f activity was minimal.

Image acquisition for dose-response experiments:

Dose-dependent GCaMP6f dynamics were captured using a 60x, 1.2 N.A. objective (Nikon), 920 nm excitation, and a 525/50 nm emission filter. Images were acquired using a 512 × 512 pixel field-of-view (FOV), 0.34 μm/pixel spatial resolution, and 1.42 Hz frame rate. Spontaneous GCaMP6f dynamics were recorded during a 1-minute baseline prior to pipetting HA into the recirculating ACSF bath.

Image acquisition for H1R pharmacology experiments:

H1R-dependent GCaMP6f dynamics were captured as described, but using a 20x, 1.0 N.A. objective (Olympus), for a spatial resolution of 1.04 μm/pixel.

Image acquisition for H1R cKO experiments:

GCaMP6f or jRGECO dynamics were captured as described for pharmacology experiments. Cre-RFP fluorescence was imaged immediately after GCaMP6f imaging using 1040 nm excitation for 600 frames at 1.42 Hz. For NE experiments on untreated slices, jRGECO dynamics were captured using 1000 nm excitation at 1.42 Hz and Cre-GFP fluorescence was imaged immediately after jRGECO imaging using 920 nm excitation for 600 frames at 1.42 Hz.

Image acquisition for GRAB-ATP:

Extracellular ATP dynamics were captured using a 20x, 1.0 N.A. objective (Olympus), 920 nm excitation, and a 525/50 nm emission filter. Images were acquired using 256 × 256 pixel FOV, 2.08 μm/pixel spatial resolution, and 5.62 Hz frame rate. To record spontaneous ATP release rate in the slice, a 5-minute baseline was recorded prior to pipetting HA into the recirculating ACSF bath.

Pharmacology

Details for pharmacological reagents used in *ex vivo* imaging experiments are as follows: HA (Sigma-Aldrich, H-7250) was dissolved in ACSF prior to each experiment and pipetted into a 10–20 mL recirculating ACSF bath for a final HA concentration of 0.5, 5, 50, or 100 μM. NE (Sigma-Aldrich, A7256) solution was pipetted into the ACSF bath for a final NE concentration of 10 μM. The H1R-specific antagonist chlorpheniramine (Sigma-Aldrich, C3025) was used at 50 μM and Tetrodotoxin Citrate (Hello Bio, HB1035) was used at 1μM. Slices were incubated in inhibitors for > 5 minutes prior to 2P imaging.

2P fluorescence event detection

GCaMP6f and jRGECO 2P videos were characterized using AQuA software[85] and custom MATLAB code. Before AQuA analysis, 2P videos were smoothed by averaging every 2-4 frames to reduce noise. For accurate detection of fluorescent events, signal detection thresholds were manually adjusted for each 2P video using AQuA's graphical user interface, keeping parameters similar within each experiment.

For GCaMP6f or jRGECO analysis in H1R cKO slices, WT and H1R cKO ROIs were

manually drawn based on co-expression patterns of the tagged Cre and the Ca^{2+} indicator, which were determined by overlaying GCaMP6f and RFP (or jRGECO and EGFP) z-projections. To make a ROI map for AQuA detection, ROIs were overlaid and filled on a black background (512 × 512 pixels). This image was flattened and converted to an 8-bit image, which was saved as a tiff and loaded into AQuA for ROI-specific event detection.

2.5.4 AQuA output analysis

After event detection, AQuA results were quantified using custom MATLAB code for each experimental condition. The key analysis steps are described below.

Dose-response data:

Percent of active pixels in Figure 2.4.1 was defined as number of AQuA detected pixels per frame relative to total pixels in the field of view. Baseline activity was defined as average % active pixels prior to HA addition. The baseline was subtracted from % active pixels to obtain Δ pixels active over time. For each slice, the maximum Δ pixels active was found, and the area under the Δ pixels active curve (AUC) was calculated across the 120 s period post-HA. Statistical differences between AUC or maximum Δ pixels active for each HA concentration were detected using MATLAB's one-sided Wilcoxon rank-sum test.

Pharmacology data:

The Δ pixels active over time and maximum Δ pixels active in Figure 2.4.3 were calculated as above. Maximum Δ pixels active for no-antagonist and +H1R-antagonist conditions were compared using MATLAB's one-sided Wilcoxon rank-sum test. To analyze Ca^{2+} event

characteristics, events pre-HA (120s period during baseline) and post-HA (120s immediately following HA) were pooled from all slices. Mean and 95% confidence interval for event amplitude, area, and duration were estimated using bootstrapping (10,000 samples with replacement) for no-antagonist and +H1R-antagonist data. Statistically significant differences between pre- and post-HA conditions were detected via a permutation test (1,000 permutations) on pooled data before bootstrapping.

H1R cKO Ca^{2+} data:

The Δ pixels active over time and maximum Δ pixels active in Figure 2.4.6 were calculated as above with the following change. The % active pixels was calculated relative to the total number of pixels subsumed by either all WT or cKO ROIs, instead of total number of pixels in the FOV. MATLAB's one-sided Wilcoxon signed-rank test was used to detect statistically significant differences between WT and cKO maximum Δ pixels active post-HA or post-NE.

ATP data:

Because GRAB-ATP events were infrequent, 1-minute bins were used to assess changes in ATP event rate. A sliding 4-minute window was used to calculate changes in mean ATP event rate across the recording, relative to the baseline mean (event rate during the 4 minutes pre-HA). In this analysis, WT slices with no antagonist showed a significant increase in ATP events during the last 4 minutes of the 2P recording relative to the baseline period. We therefore defined the post-HA period as the last 4-minute bin and conducted the same analysis for the WT + H1R antagonist and H1R cKO conditions.

2.5.5 Validation of H1R cKO

Deletion of H1R transcripts in Cre-RFP+ astrocytes was verified using RNAscope and immunohistochemistry (IHC) as follows: Neonatal virus injections were done as described to drive Cre-RFP expression in cortical astrocytes. Mice (~P28) were deeply anesthetized with vaporized isoflurane (1–1.5% vol.) and then intracardially perfused with ~10 mL of ice-cold 1X PBS and then ~10 mL of ice-cold 4% PFA. The brain was dissected out, fixed in 4% PFA overnight at 4°C, incubated in 30% sucrose at 4°C until no longer floating, and then embedded in OCT and stored at -80°C. A cryostat was then used to collect 14-20 μm sections from V1, which were stored at -80°C.

H1R mRNA probe design:

Probe design was based on the sequence deletion in H1R cKO mice. ACDBio designed and generated an RNAscope probe that targeted bases 269–1342 in the H1R gene sequence (GenBank accession #: NM_001410031.1).

H1R mRNA, S100β, and Cre-RFP labelling:

Sections were thawed to RT and washed for 5 min in 1X PBS in a Coplin jar (container used for all washes unless specified). Slides were then baked for 15 min at 60°C in a dry air oven (used for all incubations above RT). Sections were dehydrated for 5 min each in RT serial dilutions of ethanol (EtOH): 50%, 70%, and 100%. Sections were air dried for 5 min and then incubated in 2–3 drops of ACDBio H_2O_2 for 10 min at RT. After two washes in de-ionized H_2O (diH_2O), sections were washed in 100% EtOH and air dried. A pap pen was used to draw a hydrophobic barrier around each section. The barrier was allowed to dry, and sections were incubated for 15 min at

40°C in 2–3 drops (per section) of ACDBio protease III solution. Sections were washed 3 times in diH_2O at RT. Then ~50 µl of ACDBio H1R mRNA probe was added to each section and hybridized for 2 hours at 40°C. During hybridization the following reagents were brought to RT: ACDBio AMP1–3 solutions, HRP-C1, HRP blocker, and 1:1000 690 Opal dye in ACDBio TSA buffer. After hybridization, sections went through the following incubation steps and between each step sections were washed 3x in ~500µl per section of ACDBio wash buffer: 1) 2–3 drops of AMP-1 for 30 min at 40°C; 2) 2–3 drops AMP-2 for 30 min at 40°C; 3) 2–3 drops AMP-3 for 15 min at 40°C; 4) 2–3 drops of HRP-C1 for 15 min at 40°C; 5) ~50µL of 1:1000 690 Opal dye for 30 min at 40°C; 6) 2–3 drops HRP blocker for 15' at 40°C. Next, sections were processed for IHC. Sections were permeabilized and blocked by incubating for 60 min at RT in ~200 µl of antibody incubation solution (AIS: 1X PBS with 0.05% Triton X-100, 3% fetal bovine serum, 0.025% sodium azide). AIS was removed and sections were incubated overnight at 4°C in 50–75 µL of primary antibody mixtures diluted in AIS: 1:250 rabbit α S100β (Sigma-Aldrich, SA-85500172), 1:1000 rat α mCherry (Invitrogen, M11217). Sections were washed 3x in 1X PBS, 10 min each at RT. Then, sections were incubated for 2 hours at RT in 50–75µl of secondary antibody mixtures diluted in AIS: 1:2000 goat α rabbit 488 (Invitrogen, A11034), 1:2000 goat α rat 555 (Invitrogen, A21434). Sections were washed 3x in 1X PBS, 10 min each at RT and then incubated in 2–3 drops of ACDBio DAPI for 30 s at RT. Slides were gently tapped to remove DAPI, and Fluoromount (SouthernBiotech, 0100-01) was pipetted onto each section. Finally, a coverslip was added to each slide and labelled sections were stored at 4°C until imaging.

RNAscope and IHC image collection and analysis:

A Zeiss LSM 880 point-scanning confocal microscope was used to image RNAscope and IHC

labelling. Z-stacks approximately spanning each section were collected using a 63x, 1.4 N.A. oil immersion objective. All images had a 512 × 512 pixels FOV and 16-bit depth. H1R mRNA, RFP, S100β, and DAPI were imaged using 633, 561, 488, and 405 nm lasers, respectively. For each section, 1–3 FOVs were imaged across V1 layers. After image collection, laser channels were separated, and ROIs were drawn around easily identified astrocyte soma based on RFP and S100β signal. ROIs were then overlaid on H1R mRNA images (633 nm channel), and H1R puncta within ROIs were manually counted based on colocalization with S100β and RFP signal.

IHC and colocalization analysis of NeuN/Cre-RFP:

To verify lack of neuronal Cre-RFP expression, we used the above IHC procedure to co-label neurons and RFP expression in sections from $H1R^{fl/fl}$ mice that were neonatally injected with *AAV5-GFAP(0.7)-RFP-T2A-iCre,* as described above. For primary antibody labelling, we used 1:1000 rat α mCherry (Invitrogen, M11217) and 1:1000 rabbit α NeuN (EMD Millipore Corp, ABN78) to label RFP expressing cells and neurons, respectively. For secondary antibody labelling, we used 1:2000 goat α rabbit 488 (Invitrogen, A11034), 1:2000 goat α rat 555 (Invitrogen, A21434). After mounting, z-stacks were collected as described above using a 20x, 0.8 N.A. air immersion objective. RFP, NeuN, and DAPI were imaged using 561, 488, and 405 nm lasers, respectively. For image analysis, laser channels were separated, summed z-projections were generated, and ROIs were manually drawn around RFP+ soma. In ImageJ, the RFP and NeuN channels were smoothed using the Gaussian blur filter (sigma radius = 1.00) and then binarized. Somatic ROIs were overlaid on each binarized image and the % of NeuN and RFP+ positive pixels (relative to total ROI pixels) was calculated for each ROI.

CHAPTER 3

H1R MODULATES ASTROCYTE CA^{2+} AND EXTRACELLULAR ADENOSINE DYNAMICS DURING REM SLEEP

3.1 INTRODUCTION

A growing body of evidence shows that astrocytes contribute to regulation of arousal and sleep/wake. Several studies have shown that increased astrocyte Ca^{2+} generally promotes neuronal synchrony and facilitates NREM sleep[37,101], which is characterized by increased cortical oscillatory power in the delta frequency range (0.5–4 Hz). This sleep-promoting effect is thought to be mediated by adenosine, given that astrocyte Ca^{2+} drives increased extracellular adenosine[61], which is known to promote cortical delta oscillations[29,31] and regulate sleep homeostasis[26,27]. Compellingly, *in vivo* studies using astrocyte-specific genetic manipulations further suggest that astrocytic regulation of adenosine release leads to changes in sleep/wake and underlying cortical dynamics[53–56].

While astrocytes have been shown to regulate cortical synchrony and extracellular adenosine levels, two modulators of arousal, it is unclear which endogenous sleep/wake signals are required for astrocytic regulation of adenosine and cortical neurons. Building on our results presented in Chapter 2, which demonstrate that histaminergic activation of H1R drives astrocyte Ca^{2+} elevations and regulates extracellular ATP in cortex, we next investigated how astrocytic H1R shapes *in vivo* astrocyte Ca^{2+}, cortical arousal, and extracellular adenosine (ATP metabolite) dynamics. We used a cortically targeted viral strategy to delete H1R specifically in astrocytes, and then recorded astrocyte Ca^{2+} and extracellular adenosine dynamics using fiber photometry, while recording sleep/wake via EEG recordings. In summary, we found that astrocyte-specific H1R

deletion altered REM-specific astrocyte Ca^{2+}, cortical arousal, and extracellular adenosine dynamics, suggesting that astrocytic H1R signaling shapes astrocyte activity across many minutes and beyond the acute period of H1R stimulation, since HA is not released during REM. This has important implications for understanding how neuromodulators work synergistically to regulate astrocytic control of arousal, as well as the time scales over which these interactions may take place.

3.2 RESULTS

3.2.1 H1R cKO disrupts astrocyte Ca^{2+} dynamics around transitions between NREM and REM

Having established that HA drives cell-autonomous astrocyte Ca^{2+} responses in cortical slices (Chapter 2), we next tested how astrocytic H1R signaling shapes *in vivo* astrocyte Ca^{2+} dynamics across sleep and wake states. As histaminergic neurons fire tonically during wake and are almost silent during NREM and REM sleep[63–66], we hypothesized that astrocytic H1R deletion would lead to reduced astrocyte Ca^{2+} activity specifically during wake. To test this, we genetically deleted H1R uni-hemispherically in cortical astrocytes by virally co-expressing astrocyte-specific Cre and jRGECO in V1 of adult $H1R^{fl/fl}$ mice, and implanted an optical fiber directly over the virus injection site (Fig. 3.4.1A and Fig. 3.4.5A–B). We also implanted an EEG screw in contralateral V1 to track cortex-wide sleep/wake states (Fig. 3.4.1A and Fig. 3.4.5A). Two weeks after the virus injections, we measured astrocyte jRGECO dynamics via fiber photometry across sleep/wake in freely moving mice (Fig. 3.4.1B).

We used a Hidden-Markov model to score sleep/wake periods and observed that both genotypes exhibited well-established wake-, NREM-, and REM-specific patterns in EEG

dynamics (Fig. 3.4.2B–E). Both WT and cKO mice exhibited elevated delta and reduced theta power during NREM relative to wake and REM (Fig. 3.4.2C). Additionally, while we saw no difference in theta power during wake versus REM when comparing mean power across bouts (Fig. 3.4.2C), both WT and cKO mice exhibited higher theta power at NREM-to-REM relative to NREM-to-wake transitions (Fig. 3.4.2D–E). Finally, each genotype exhibited similar sleep/wake architecture, with a small difference in percent of individual EEG recordings successfully scored (Fig. 3.4.2F, 93.0% for WT versus 95.5% for cKO) and a difference in percent time spent in NREM (Fig. 3.4.2G, 45.5% for WT versus 48.7% for cKO).

Since astrocytes respond via Ca^{2+} to multiple wake-specific signals including HA, NE, dopamine, acetylcholine, and glutamate[16], we predicted that the H1R cKO animals would show an attenuation of wake-specific astrocyte Ca^{2+} activity, rather than a complete blockade. To quantify Ca^{2+} activity, we used a peak-finding function to characterize peak amplitude and frequency during wake, NREM, and REM in WT and cKO mice (Fig. 3.4.1B). Consistent with published data, both genotypes exhibited increased astrocyte Ca^{2+} peak amplitude and frequency during wake relative to NREM (Fig. 3.4.1B–D). We also saw increased Ca^{2+} levels during REM relative to NREM, in contrast to that observed in somatosensory and prefrontal cortices[48,49]. Finally, peak frequency increased during REM relative to wake in both genotypes (Fig. 3.4.1D), which likely reflects the increase in Ca^{2+} at REM-onset (Fig. 3.4.1F) and the short duration of REM periods compared to wake periods (Fig. 3.4.1B and Fig. 3.4.2G). Contrary to our hypothesis, we found that wake-specific astrocyte Ca^{2+} peak frequency was increased in cKO mice relative to WT (Fig. 3.4.1D). Since our *ex vivo* data demonstrated that astrocytic H1R drives increased Ca^{2+} activity, we were surprised to see that H1R cKO animals exhibited more Ca^{2+} activity—as measured by frequency—during wake when extracellular HA levels are high. This result suggests that H1R activity in

astrocytes modulates how these cells respond to other wake-specific signals, which is consistent with the differences in *ex vivo* WT and cKO astrocyte Ca^{2+} responses to NE following stimulation with HA (Fig. 2.4.6B, D).

In addition to quantifying astrocyte Ca^{2+} during entire sleep/wake periods, we also measured changes in astrocyte Ca^{2+} across sleep/wake transitions, using the absolute change in jRGECO fluorescence relative to mean jRGECO fluorescence during the pre-transition period. Consistent with previous data[43,48–50], both genotypes exhibited a clear increase in Ca^{2+} at the transition from NREM-to-wake and a decrease at the wake-to-NREM transition (Fig. 3.4.1E), and this Ca^{2+} activity did not differ between the two genotypes during either transition (Fig. 3.4.1E, G). However, genotype-specific differences in Ca^{2+} dynamics were apparent at NREM-to-REM and REM-to-NREM sleep transitions (Fig. 3.4.1F), an unexpected finding since extracellular HA levels in cortex are low during NREM and lowest during REM[63]. (Note that we only present data from NREM/REM transitions, since we did not observe REM-to-wake transitions.) Specifically, WT mice exhibited a larger increase in Ca^{2+} during REM-onset and a larger decrease with REM-offset compared to cKO mice, which we quantified by comparing the area under the curve (AUC) during the 60s following REM-onset or offset (Fig. 3.4.1H). The AUC for each transition type was decreased in cKO compared to WT mice, indicating that cKO astrocyte Ca^{2+} has a narrower dynamic range around NREM/REM sleep transitions. These results suggest that HA activation of astrocytic H1R during wake may have effects on astrocyte physiology beyond the immediate time frame of HA release and into subsequent sleep periods.

3.2.2 Astrocyte-specific H1R activity in cortex contributes to REM sleep regulation

HA promotes arousal via H1R activation[68] and astrocyte-specific H1R contributes to the wake-promoting effects of this receptor when examined in a brain-wide manner[79]. However, whether cortical astrocytic H1R deletion is sufficient to shape neuronal dynamics underlying sleep/wake remained untested. We therefore targeted genetic deletion of astrocytic H1R to the cortex and measured effects on cortical arousal and sleep/wake behavior. To do this, we injected either an astrocyte-specific Cre or a sham virus into V1 of $H1R^{fl/fl}$ mice, to generate H1R cKO and negative control mice (WT mice), respectively. An EEG screw was implanted directly over the virus injection site to track cortical dynamics at the site of astrocytic H1R deletion across sleep/wake (Fig. 3.4.3A and Fig. 3.4.5C–H).

Using the Hidden-Markov model to score sleep/wake periods as above, almost the entirety of each recording was classified as wake, NREM, or REM, with an average of 96.3% and 96.9% of each recording scored for WT and cKO mice, respectively. WT and cKO mice spent an average of 60.8% of the recording time in wake, 37.1% in NREM, and 2.1% in REM, with no differences detected between genotypes (Fig. 3.4.3B). Each genotype also exhibited similar bout durations for wake and NREM states, with overall means of 9.1 and 6.9 minutes, respectively (Fig. 3.4.3B). However, consistent with REM-specific changes in cKO astrocyte Ca^{2+} described above, cKO mice exhibited shorter REM bouts (0.7 ± 0.2 minutes) relative to WT mice (1.1 ± 0.1 minutes, Fig. 3.4.3B).

We next assessed cortical dynamics across sleep/wake. When comparing power spectral densities (PSD), frequencies spanning 1–20 Hz were similarly represented in WT and cKO mice during wake and NREM periods, but we observed genotype-specific differences in the delta and theta frequency ranges for REM PSDs (Fig. 3.4.3C). We further quantified cortical dynamics by

comparing percent power in the delta (1–4 Hz), theta (6–10 Hz), and sigma (10–15 Hz) frequency bands relative to total power in wake, NREM, or REM (Fig. 3.4.3D). As expected, we saw no difference in band power during wake and NREM. However, we found that cKO mice exhibited a small but significant increase in delta power specifically during REM periods (~24% in WT versus ~27% in cKO, Fig. 3.4.3D), which aligns with the SWA promoting effects of astrocyte Ca^{2+} and the increase in wake-specific Ca^{2+} peak frequency in H1R cKO mice (Fig. 3.4.1D).

3.2.3 Astrocyte-specific H1R modulates REM-specific adenosine dynamics in cortex

Astrocytes can increase cortical synchrony, a marker of reduced arousal, by promoting adenosine-mediated neuronal inhibition[53,55,102]. Further, neuromodulatory input may play key roles in shaping astrocyte-adenosine signaling[36,82]. Thus, we compared extracellular adenosine levels in WT and H1R cKO mice using fiber photometry recordings of the extracellularly facing fluorescent adenosine sensor, GRAB-Adenosine (GRAB-Ado)[103] in V1, while simultaneously tracking sleep/wake states via an EEG screw in contralateral V1 (Fig. 3.4.4A–B).

For both WT and cKO animals, GRAB-Ado levels in cortex were high during wake and low during NREM and REM sleep according to the distribution of z-scored GRAB-Ado fluorescence (Fig. 3.4.4B–C), consistent with measurements in basal forebrain using GRAB-Ado[51,104]. Differences between the two genotypes were observed during REM sleep, with cKO mice exhibiting lower overall GRAB-Ado levels relative to WT (Fig. 3.4.4C). In cKO mice only, REM-specific GRAB-Ado was also lower than NREM GRAB-Ado (Fig. 3.4.4C).

Consistent with differences in Ca^{2+} activity during REM-related state transitions (Fig. 3.4.1), we observed distinct WT and cKO GRAB-Ado dynamics at NREM/REM sleep transitions, whereas no genotype-specific differences were detected for NREM/wake transitions (Fig. 3.4.4D–

E). Compared to WT, cKO mice exhibited larger decreases in GRAB-Ado levels at NREM-to-REM transitions and larger increases in GRAB-Ado levels at REM-to-NREM transitions, as assessed by change in fluorescence relative to pre-transition period (Fig. 3.4.4F) and AUC during the 60s post either REM- or NREM-onset (Fig. 3.4.4G). These results are consistent with overall reduced GRAB-Ado levels during REM in the cKO relative to WT (Fig. 3.4.4C). Overall, we found that extracellular adenosine levels in cortex increased throughout wake, decreased during NREM, and transiently decreased further with REM-onset. Further, our results show that astrocytic H1R activity narrows the dynamic range of extracellular adenosine fluctuations specifically across NREM/REM sleep transitions.

3.3 DISCUSSION

3.3.1 H1R signaling modulates astrocyte activity *in vivo*

Astrocytes exhibit highly heterogeneous Ca^{2+} activity across arousal states, with increased activity during wake compared to sleep that is driven, at least in part, by noradrenergic input[38–40,83,94]. Despite the expression of many different neuromodulatory GPCRs in astrocytes, how non-adrenergic neuromodulators regulate astrocytic Ca^{2+} dynamics specific to wake, NREM, and REM remains largely unknown. Our understanding of REM-specific astrocyte Ca^{2+} dynamics is particularly limited, with Ca^{2+} increasing at NREM-to-REM in basal forebrain[51], but decreasing in somatosensory[49] and frontal cortex[48].

Here, astrocyte-specific H1R deletion altered Ca^{2+} dynamics *in vivo* with notable effects on Ca^{2+} during REM sleep (Fig. 3.4.1), establishing that HA directly activates astrocyte Ca^{2+} in behaving animals. In these experiments, we used a viral Cre/lox strategy to conditionally delete H1R, which allowed us to specifically target cortical astrocytes and avoid neuronal Cre

expression[105,106], although it resulted in jRGECO photometry signals from a mixture of WT and cKO astrocytes. Therefore, we suggest that our results are an underestimate of the full extent to which H1R modulates astrocyte Ca^{2+} *in vivo.* Despite mosaic H1R deletion, we observed significant changes in astrocyte Ca^{2+} activity during specific sleep/wake stages. Given our *ex vivo* data showing that H1R deletion reduces astrocyte Ca^{2+} responsiveness to HA, it was notable to find that H1R cKO mice displayed 1) *increased* Ca^{2+} peak frequency during wake, when HA is released, and 2) altered relative Ca^{2+} levels around NREM/REM transitions, when extracellular HA levels are low. These changes suggest that H1R activity shapes how astrocytes respond to non-histaminergic inputs, such as NE during wake and acetylcholine during REM, which would be consistent with our *ex vivo* data (Fig. 2.4.6B) and with published evidence that prior astrocyte Ca^{2+} activity influences ongoing dynamics[83,86,100]. Long-term changes occurring across sleep/wake states that underly the effect of H1R activity could include Ca^{2+}-dependent modulation of protein expression or GPCR signaling.

Both the WT and cKO animals exhibited increased astrocyte Ca^{2+} at NREM-to-REM transitions (Fig. 3.4.1G), which is inconsistent with data from other cortical areas[48,49]. This discrepancy aligns with evidence that astrocyte Ca^{2+} dynamics can differ among cortical areas, for example when examining locomotion-induced Ca^{2+} in V1 vs. prefrontal cortex[15]. Our results also align with reports of higher neuronal activity in V1 during REM sleep relative to somatosensory and motor cortices[107]. In this context, our results suggest that H1R signaling might shape REM-specific astrocyte Ca^{2+} activity that is likely driven by a combination of acetylcholine and glutamate released locally by REM-active neurons in V1, and further supports an emerging appreciation for astrocyte heterogeneity across the brain.

Overall, our results indicate that H1R activity may shape astrocyte to responses to other neuromodulators over extended timescales, leading to changes in Ca^{2+} activity even when HA is not released, such as during REM sleep.

3.3.2 Astrocytic H1R signaling modulates extracellular adenosine and cortical dynamics during REM sleep

Astrocytes can regulate neuronal dynamics via NE-triggered adenosine release[11–14], suggesting that neuromodulators may stimulate changes in astrocyte-adenosine signaling to modulate arousal. We therefore measured extracellular adenosine dynamics across sleep/wake in WT and H1R cKO cortex using GRAB-Ado. Our results confirm what has been observed in microdialysis studies, where cortical extracellular adenosine increases across wake periods and falls during NREM sleep[28]. Due to the limited temporal resolution of microdialysis, the dynamics of cortical adenosine during relatively short REM periods were previously unclear — an important gap in understanding, especially considering the hypothesized role of cortical adenosine dynamics in arousal control. We show here that extracellular adenosine markedly drops at NREM-to-REM transitions and begins to increase prior to NREM onset following REM (Fig. 3.4.4G), thereby revealing a more complete picture of extracellular adenosine fluctuations across sleep/wake.

Astrocytic H1R deletion altered REM-specific adenosine dynamics, consistent with the H1R-dependent changes in astrocyte Ca^{2+} observed during REM (compare Fig. 3.4.1G–H and Fig. 3.4.4F–G). Astrocytic H1R deletion increased the relative drop and rise in extracellular adenosine at the NREM-to-REM and REM-to-NREM transitions, respectively. Thus, H1R cKO mice exhibited a larger dynamic range for adenosine fluctuations around REM/NREM transitions, which accompanies a reduced dynamic range in astrocyte Ca^{2+} around these transitions. The

correlation between larger adenosine fluctuations and smaller Ca^{2+} fluctuations in the cKO suggests that astrocyte Ca^{2+} during REM might limit decreases in extracellular adenosine by stimulating astrocytic ATP release or modulating adenosine uptake/metabolism, although this idea remains to be tested.

Along with REM-specific changes in adenosine and Ca^{2+}, we also observed increased delta power during REM sleep (Fig. 3.4.3D–E). Interestingly, cKO mice exhibited increased delta during REM that accompanied increased astrocyte Ca^{2+} peak frequency during wake (Fig. 3.4.1), indicating a link between wake-specific astrocyte Ca^{2+} and changes in cortical dynamics during sleep. This is consistent with evidence that GPCR stimulated astrocyte Ca^{2+} can lead to changes in neuronal dynamics that persist for over an hour[108], more specifically astrocyte Ca^{2+} activation during wake can increase delta power during NREM sleep[43]. While intriguing, establishing a functional link between wake-specific H1R triggered Ca^{2+} and changes in REM sleep requires further investigation.

Whether there is a consequential mechanistic link between increased delta during REM and decreased REM-specific adenosine levels observed in the cKO mice remains unclear. Since high extracellular adenosine promotes delta power during NREM sleep[26,27,109], one might expect to see increased delta power coincide with increased extracellular adenosine during REM, however we see the opposite (Fig. 3.4.3D, E and Fig. 3.4.4C, F). This discrepancy suggests that extracellular adenosine might have distinct effects on population-wide neuronal dynamics during different behavioral states, which could be explained by the unique combinations of neuromodulators that characterize wake, NREM, and REM. Alternatively, it is possible that EEG recordings lack the spatial resolution necessary to accurately detect the neuronal changes mediated by shifts in extracellular adenosine, which were measured using fiber photometry, a technique that captures

relatively localized changes in fluorescence. *Ex vivo* electrophysiological experiments in WT and H1R cKO slices could illuminate in necessary detail how astrocytic H1R signaling modulates adenosine-dependent changes in state-specific neuronal activity.

Overall, our results reveal that extracellular adenosine levels in cortex transiently decrease during REM periods and suggest that astrocytic H1R signaling shapes REM-specific extracellular adenosine and cortical dynamics. We note that the local nature of photometry measurements complicates direct correlations with more cortex-wide EEG recordings. Future experiments employing spatially localized recording techniques—such as optrodes[110]—could better elucidate the correlation between H1R-dependent adenosine fluctuations and cortical oscillatory dynamics. While we have identified relationships between astrocyte-specific H1R signaling and various aspects of arousal, the mechanistic links underlying these findings remain unclear. Nonetheless, our results raise critical questions about the role of astrocytes in REM sleep regulation, particularly through neuromodulatory signaling and downstream adenosine pathways. Addressing these gaps is vital, given how little is known about the relationship between astrocyte physiology and REM sleep.

3.4 FIGURES

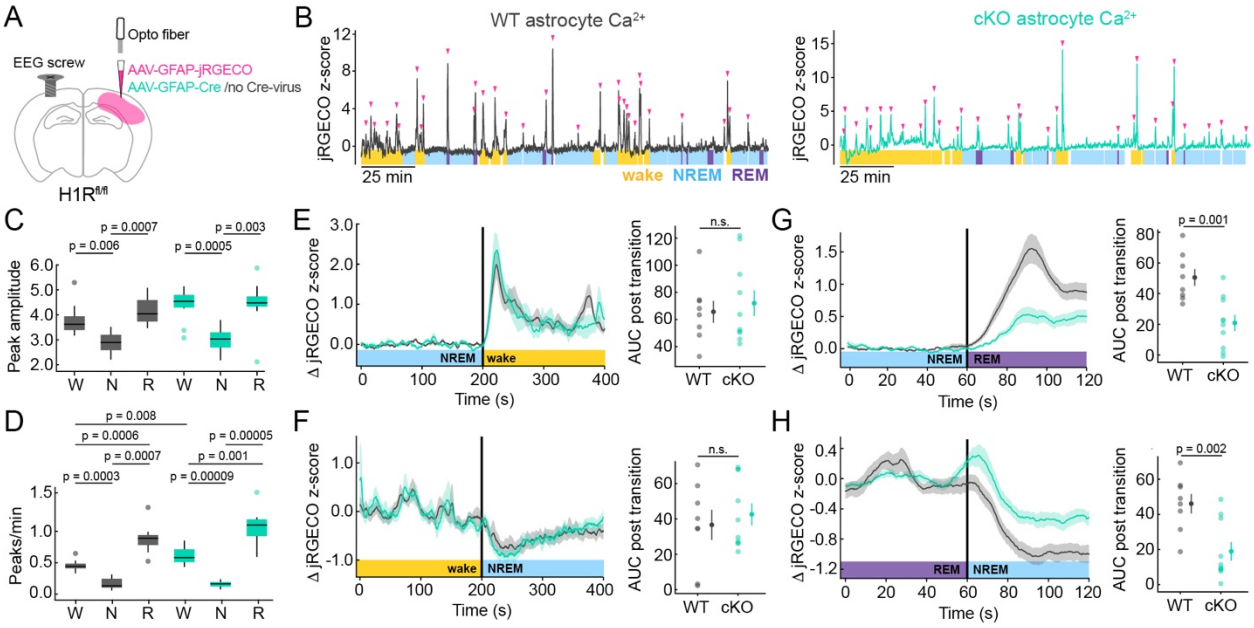

Figure 3.4.1. Astrocytic H1R cKO specifically disrupts astrocyte Ca^{2+} dynamics during wake and around REM sleep transitions.
(A) Conditional H1R knockout mouse surgery schematic shows astrocytic jRGECO and Cre-GFP viral injections into V1, photometry fiber placement, and contralateral EEG screw placement in $H1R^{fl/fl}$ mice. Wild-type surgeries omitted Cre virus. **(B)** Example z-scored jRGECO photometry traces from WT (left, grey) and H1R cKO (right, cyan) mice aligned to color-coded wake, NREM, and REM periods. White blocks in sleep/wake scoring indicate periods that were not successfully scored by HMM. Horizontal scale bar = 25 minutes. **(C)** Distribution of jRGECO peak amplitudes during wake, NREM, and REM in WT and H1R cKO mice. Peaks detected using Python's signal.find_peaks function with prominence level = 2, distance = 5s, width = 1s. p-values calculated via one-side Wilcoxon rank-sum test. **(D)** Distribution of jRGECO peaks per minute during wake, NREM, and REM in WT and H1R cKO. p-values calculated via one-side Wilcoxon rank-sum test. **(E–H)** Event-triggered averages of change in jRGECO relative to mean of pre-transition period. Traces = mean jRGECO activity. Shaded error bar = SEM. Righthand plots show mean area under the curve (AUC) following state transition for WT and cKO. AUC is integration of signal during 60s post-transition. Mean per animal with overall mean ± SEM at right. p-values calculated via one-side Wilcoxon rank-sum test. **(E)** NREM-wake transitions spanning 400s. **(F)** Wake-NREM transitions spanning 400s. **(G)** NREM-REM transitions spanning 120s. **(H)** REM-NREM transitions spanning 120s. Too few REM-wake transitions were detected in recordings for analysis.

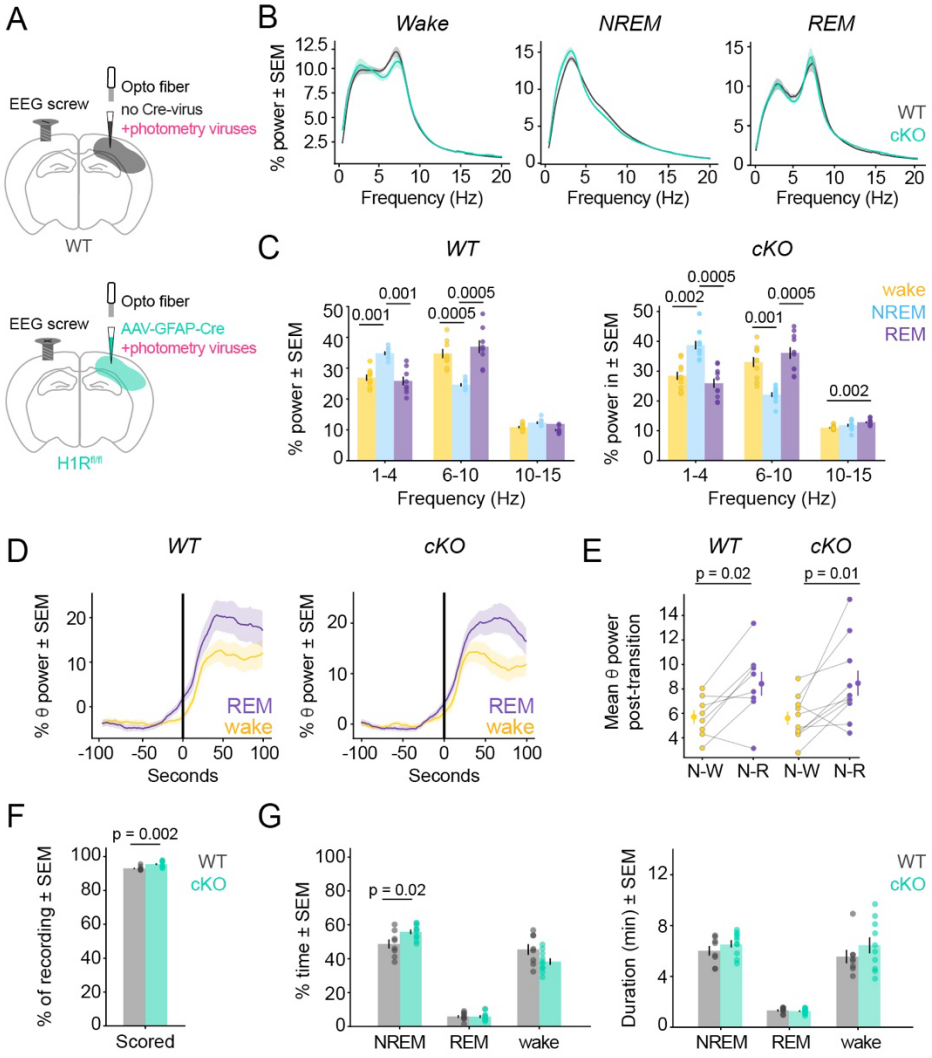

Figure 3.4.2. Sleep/wake characteristics in wild-type and H1R cKO mice with EEG screw contralateral to photometry fiber and Cre-virus.
(A) Mouse surgery schematics show location of EEG screw, photometry fiber, and virus injections in WT and H1R cKO mice. Photometry fiber was implanted over V1 injection site for astrocytic jRGECO virus ± extracellular GRAB-Ado and astrocytic Cre virus. EEG screw was implanted in contralateral V1. WT cohort included c57bl6 mice with no GRAB-Ado or Cre viruses and $H1R^{fl/fl}$ mice injected with astrocytic sham virus and GRAB-Ado virus. **(B)** Power spectral density (PSD) plots show WT (grey) and cKO (cyan) % power relative to total power across 1–20 Hz during wake, NREM, and REM. PSDs calculated via multitaper spectrogram. Traces = mean across mice; shaded error bar = SEM. **(C)** WT (left) and cKO (right) relative band power (% of total power in each state) for δ (1–4 Hz), θ (6–0 Hz), and σ (10–15 Hz) during wake (yellow), NREM (blue), and REM (purple). Overall mean and overlaid data points show mean per mouse. Error bars = SEM. p-values via Wilcoxon rank-sum test with Bonferroni correction for multiple comparisons.
(Figure caption continued on the next page.)

(Figure caption continued from the next page.)
(D) Event-triggered averages show change relative to mean of 100s pre-transition period) in θ power around NREM-wake (yellow) and NREM-REM (purple) transitions spanning 200s for WT (left) and cKO (right). Traces = mean across mice; shaded error bars = SEM. **(E)** Summary statistics in D show increased θ power at REM-onset relative to wake-onset for WT (left) and cKO (right). Scattered data points show mean (per mouse) % θ power during 100s post transition for NREM-to-wake (yellow) and NREM-to-REM (purple). Data points with error bars = overall mean ± SEM (WT N-W: 5.7 ± 0.5, WT N-R: 8.4 ± 1.0, cKO N-W: 5.6 ± 0.5, cKO N-R: 8.47 ± 1.0). p-values via one-sided Wilcoxon rank-sum test. **(F)** % of individual recordings scored via HMM as wake, NREM, or REM. Overlaid data points show mean per mouse and bars show overall mean ± SEM (WT: 93.0 ± 0.4%, cKOs: 95.5 ± 0.6%). p-value calculated via one-sided Wilcoxon rank-sum test. **(G)** Mean % time (relative to total time scored) in wake, NREM, and REM (left) and mean bout duration in minutes for wake, NREM, and REM (right). Overlaid data points show mean per mouse and bars show overall mean ± SEM. % time per state for WT: 45.4 ± 3.1 wake, 48.7 ± 2.7 NREM, 5.9 ± 0.9 REM; cKO: 38.3 ± 2.0 wake, 55.9 ± 1.4 NREM, 5.8 ± 0.8 REM. Mean bout duration (min) for WT: 5.5 ± 0.5 wake, 6.0 ± 0.4 NREM, 1.3 ± 0.1 REM; cKO: 6.4 ± 0.6 wake, 6.6 ± 0.3 NREM, 1.3 ± 0.1 REM. One-sided Wilcoxon rank-sum test shows differences between WT and cKO % time in NREM sleep.

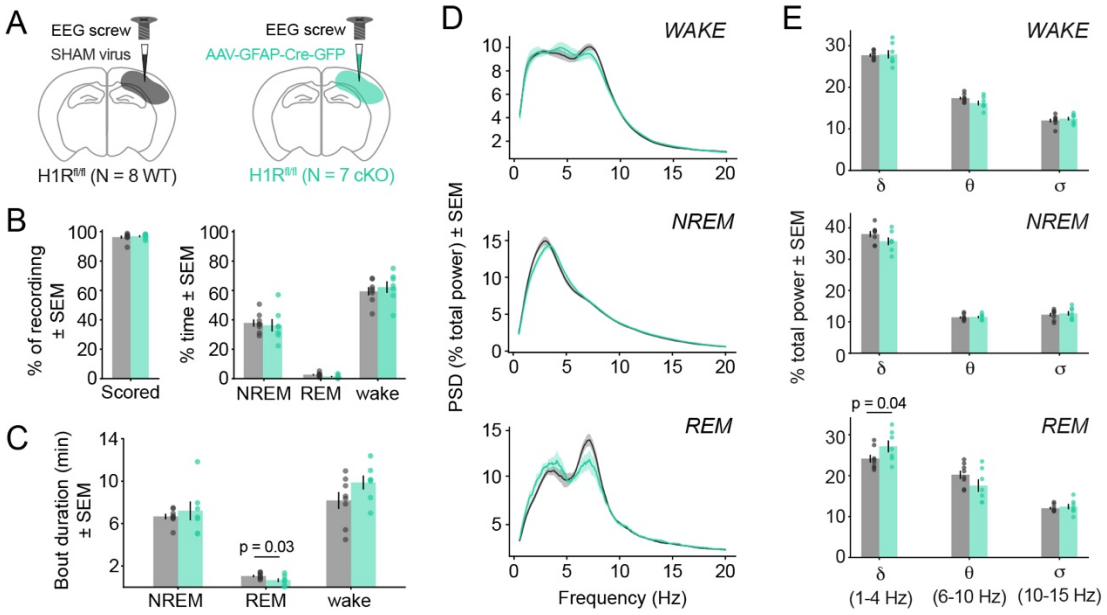

Figure 3.4.3. Unihemispheric astrocyte-specific H1R cKO alters REM sleep.
(A) Surgery schematics show V1 astrocytic Cre or sham virus injection and EEG screw location in transgenic $H1R^{fl/fl}$ mice. Mouse number in each cohort listed below schematics. Color code for experimental cohorts used in B–H. **(B–C)** WT and cKO sleep/wake architecture. For each plot, overlaid data points show mean per mouse. Bar with error bars = mean ± SEM. **(B)** Left: % individual recordings scored as wake, NREM, or REM (WT: 96.3 ± 1.0%, cKO: 96.9 ± 0.6%). Right: % time in wake, NREM, and REM (mean for WT: 59.4 ± 2.8 wake, 37.9 ± 2.4 NREM, 2.7 ± 0.4 REM; cKO: 62.2 ± 4.0 wake, 36.3 ± 4.2 NREM, 1.4 ± 0.4 REM). **(C)** Bout duration in minutes for each behavioral state (mean for WT: 8.2 ± 0.8 wake, 6.7 ± 0.3 NREM, 1.1 ± 0.1 REM; cKO: 9.9 ± 0.7 wake, 7.2 ± 0.9 NREM, 0.7 ± 0.2 REM). One-sided Wilcoxon rank-sum test detects differences between WT and cKO REM bout duration. **(D)** Power spectral density (PSD) plots show WT and cKO % power relative to total power across 1–20 Hz during wake, NREM, and REM. PSDs calculated via multitaper spectrogram. Traces = mean across mice; shaded error bar = SEM. **(E)** Bar plots show WT and cKO % band power (relative to total power in each state) for δ (1–4 Hz), θ (6–10 Hz), and σ (10–15 Hz) during wake (top), NREM (middle), and REM (bottom). Bars show overall mean and overlaid data points show mean per mouse. Error bars = SEM. One-sided Wilcoxon rank-sum test detects significant differences between WT and cKO δ power during REM (WT δ: 24.1 ± 1.0%; KO δ: 27.2 ± 1.4%).

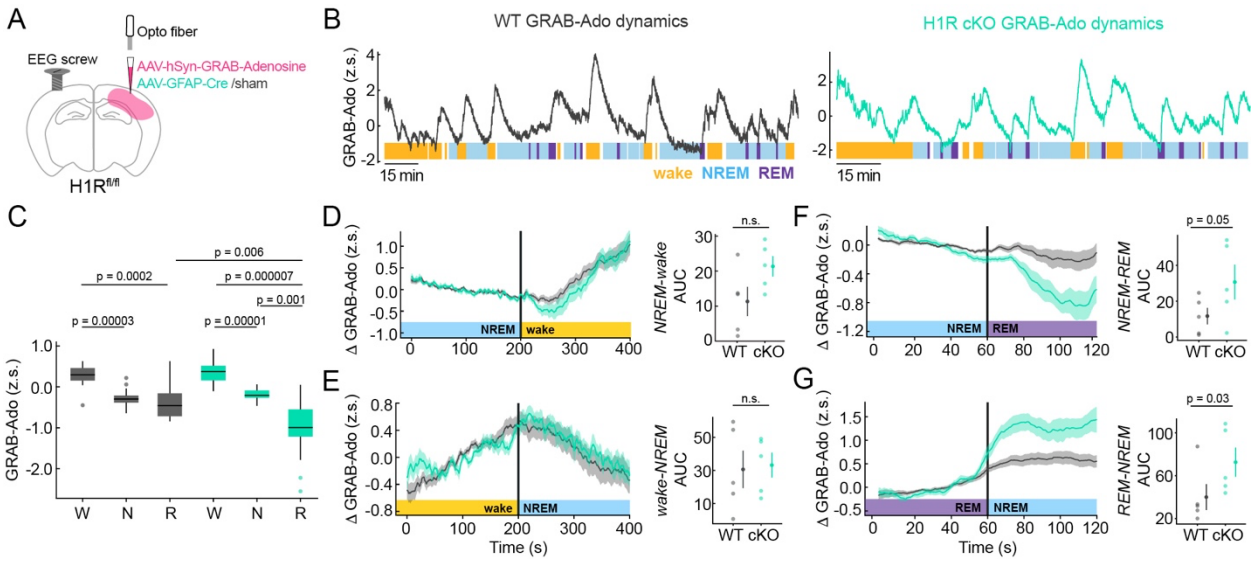

Figure 3.4.4. Astrocytic H1R activity shapes REM-specific extracellular adenosine dynamics.

(A) Conditional H1R knockout mouse surgery schematic shows extracellular GRAB-Ado and astrocytic Cre viral injections into V1, photometry fiber placement, and contralateral EEG screw placement in $H1R^{fl/fl}$ mice. WT surgeries used sham virus instead of Cre virus. H1R cKO N = 5; WT N = 5. **(B)** Example z-scored GRAB-Ado photometry traces from WT (grey) and H1R cKO (cyan) recordings aligned to color-coded wake (yellow), NREM (blue), and REM (purple) periods. White blocks in sleep/wake scoring indicate periods that were not successfully scored by HMM. Horizontal scale bar = 15 minutes. **(C)** Distribution of GRAB-Ado z-score values from wake, NREM, or REM in WT and cKO recordings. p-values via one-sided Wilcoxon rank-sum test. **(D–G)** Event-triggered averages of change in GRAB-Ado relative to mean of pre-transition period. Trace = mean across recordings. Shaded error bars = SEM. Right: mean absolute value of the area under the curve (AUC) following state transition for WT and cKO. AUC is integration of GRAB-Ado signal during 60s post-transition. Data points show mean per animal with overall mean ± SEM at right. p-values calculated via one-side Wilcoxon rank-sum test. **(D)** NREM-wake transitions spanning 400s. **(E)** Wake-NREM transitions spanning 400s. **(F)** NREM-REM transitions spanning 120s. **(G)** REM-NREM transitions spanning 120s. Too few REM-wake transitions were detected in recordings for analysis.

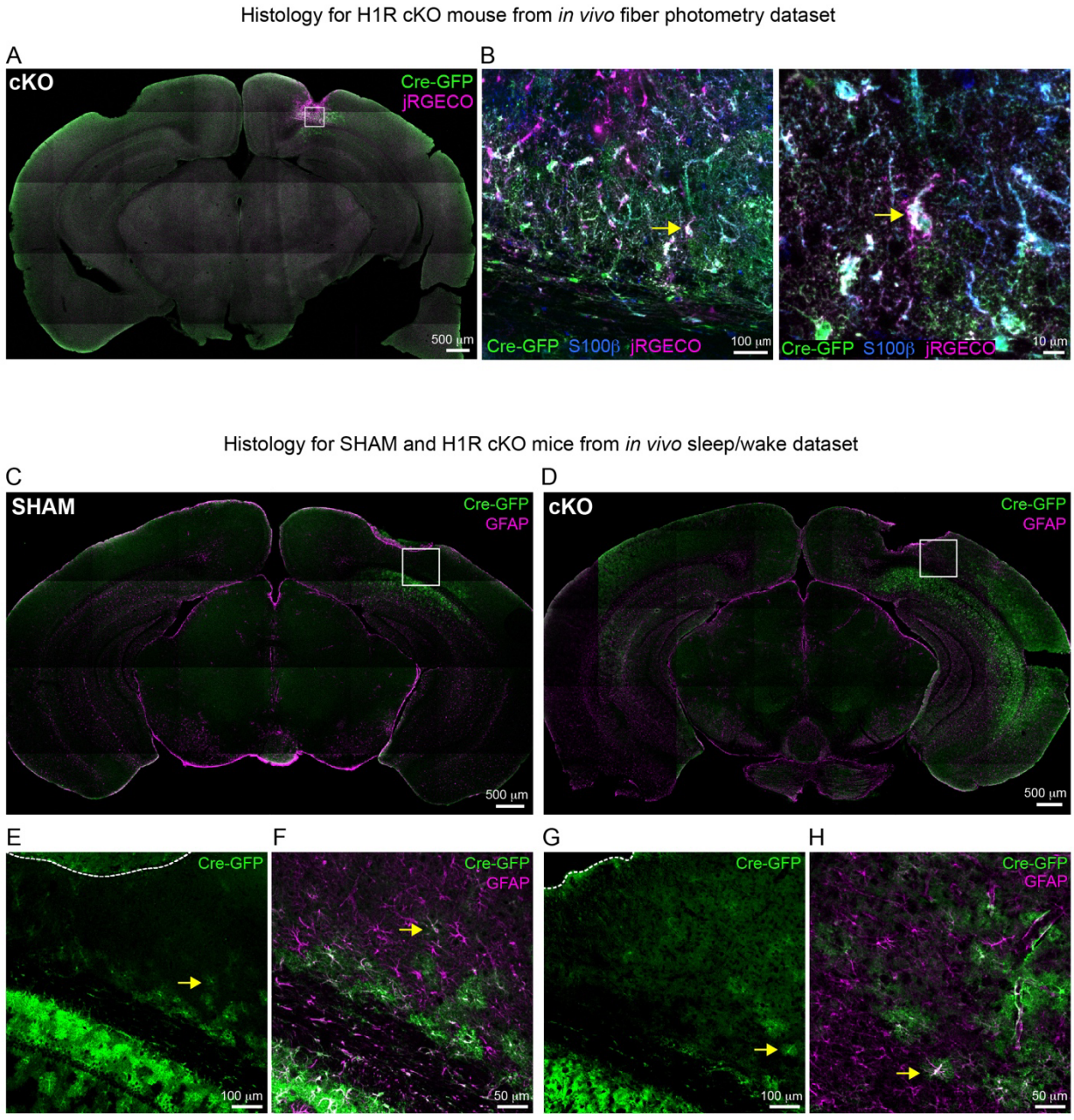

Figure 3.4.5. Localization of virus transduction, EEG screw, and photometry fiber in H1R$^{fl/fl}$ brains.
(A) Representative confocal micrograph of H1R cKO brain slice for datasets shown in Figure 3.4.1 and 3.4.2. Astrocytic Cre-GFP (green) and jRGECO (magenta) is expressed below photometry fiber track in right hemisphere. White box outlines area shown in B. EEG screw track visible in contralateral hemisphere. Scale bar = 500 µm. **(B)** Left: confocal micrograph from white boxed region in A showing Cre-GFP (green), jRGECO (magenta), and S100β (blue) expression below photometry fiber track.
(Figure caption continued on the next page.)

(Figure caption continued from the next page.)
Yellow arrow indicates $GFP^+/jRGECO^+/S100\beta^+$ astrocyte. Scale bar = 100 μm. Right: higher magnification confocal micrograph showing $GFP^+/jRGECO^+/S100\beta^+$ astrocyte indicated with yellow arrow in left image. Scale bar = 10 μm. **(C–D)** Representative confocal micrographs of sham (C) and cKO (D) brain slices for datasets shown in Figure 3.4.3. Astrocytic Cre-GFP (green) and GFAP (magenta) expression below EEG screw track visible in right hemispheres. White boxes outline areas shown in E–H. Scale bars = 500 μm. **(E–H)** Confocal micrographs in E–F and G–H show Cre-GFP (green) and GFAP (magenta) expression in white boxed regions in C and D, respectively. **(E, G)** Confocal micrograph showing astrocytic Cre-GFP expression in cortex and hippocampus below EEG screw track. Yellow arrows indicate GFP^+ astrocyte shown at a higher magnification in F and H. White dotted line = tissue edge of EEG screw track. Scale bars = 100 μm. **(F, H)** Confocal micrograph showing Cre-GFP (green) and GFAP (magenta) expression in cortical astrocytes below EEG screw track. Yellow arrows in F and H indicate $GFP^+/GFAP^+$ astrocyte in cortex shown by yellow arrows in E and G, respectively. Scale bars = 50 μm.

3.5 METHODS

3.5.1 Surgical procedures

1–2 hours before surgery, mice (see Chapter 2 for animal details) were administered dexamethasone (5 mg/kg, s.c.). At the time of surgery, mice were anesthetized with vaporized isoflurane (1–1.5% vol.) in addition to 0.05 mg/kg buprenorphine (s.c.) and 5 mg/kg carprofen (i.p.). Mice were positioned on a digital stereotax and lidocaine was administered over the surgery site (-2.5 mm lateral, +0.5 mm rostral from lambda). Following surgery, all animals were singly housed and given additional enrichment and post-operative care with close monitoring.

Fiber photometry surgery for WT and H1R cKO mice

Following anesthesia and pain management procedures described above, a craniotomy window was opened over left V1 and we subsequently injected -0.2 mm below cortex with 1000 nl viral vector mixtures at 2 nl/sec. To measure WT astrocyte Ca^{2+} and extracellular adenosine dynamics, C57BL6 mice were co-injected with *AAV9-hSyn-GRAB-Adenosine1.0* (1.0E13 vg/mL) and *AAV9-pGp-AAV-gfa(abc1d)-jRGECO1b* at a 2:1 ratio. For measuring astrocyte Ca^{2+} dynamics in H1R cKO mice, $H1R^{fl/fl}$ mice were co-injected with viral vectors *AAV5-GFAP(0.7)-EGFP-T2A-iCre* and *AAV9-pGp-AAV-gfa(abc1d)-jRGECO1b* at a 2:1 ratio. To measure astrocyte Ca^{2+} and extracellular adenosine H1R cKO mice, $H1R^{fl/fl}$ mice were co-injected with viral vectors *AAV5-GFAP(0.7)-T2A-iCre, AAV9-hSyn-GRAB-Adenosine1.0, and AAV9-pGp-AAV-gfa(abc1d)-jRGECO1b* at a 2:2:1 ratio. For all mice, a fiber optic cannula (Mono Fiberoptic Cannula, 400-µm core, 430 nm, 0.66 NA, 1 mm length, Doric Lenses) was then lowered to the depth of viral injections. To track sleep/wake in these mice, a screw electrode (8403, Pinnacle) was implanted in right V1 (-2.5 mm lateral, +0.5 mm rostral from lambda), and soldered onto a biosensor headmount

(8402, Pinnacle). A reference electrode was placed in the contralateral frontal cortex (-1.25 mm lateral, +2.70 mm rostral from bregma) and EMG probes from the headmount were inserted into the trapezius muscles. The headmount and fiber optic cannula were secured in place using dental cement (C&B Metabond, Parkell).

EEG/EMG surgery for sleep/wake behavioral data

Using $H1R^{fl/fl}$ mice, a craniotomy window was opened over right V1 and subsequently injected at -0.2 mm with 1000 nl of *AAV5-GFAP(0.7)-EGFP* or *AAV5-GFAP(0.7)-EGFP-T2A-iCre*, respectively, at 2 nl/sec. A screw electrode was implanted directly over the virus injection site and soldered onto a biosensor headmount. A reference electrode and EMG wire were implanted, and the headmount was secured as described above.

3.5.2 Fiber photometry and electrophysiology recordings

Animals were given 2 weeks post-surgery for recovery and viral expression. They were then habituated in a freely moving recording set up for at least one 2-hour session before experimental recordings began. The recording chamber was a plexiglass cylinder (height = 8 in; diameter = 10 in) filled with bedding from the animal's home cage. All cables tethered to the animal's headmount were run through a rotary joint (Doric Lenses), which was attached to a bar secured to the top of the recording chamber. Experimental recordings lasted 195 min and each animal underwent recordings at least 1–2 times per week until 5-weeks post-surgery when animals were euthanized and perfused for immunohistochemistry to validate implant locations and viral expression.

A Tucker-Davis Technologies (TDT) RZ10X processor, equipped with Lux integrated 405, 465, and 560-nm LEDs, photosensors and low autofluorescence fiber optic patch cords (400-µm

core, 0.57 NA; Doric Lenses), was used to acquire fiber photometry data through the TDT Synapse software. Fiber photometry signals were acquired using a 1017 Hz sampling rate with a 6 Hz low-pass filter through the TDT Synapse software. Simultaneously, EEG/EMG data were collected using a 1017 Hz sampling rate with a 30 Hz low-pass filter through a three-channel Pinnacle EEG/EMG Data Acquisition System connected to the TDT RZ10X processor.

3.5.3 Data analysis

Custom code written in Python (3.9.7) was used for signal processing and analyzing fiber photometry and electrophysiology data acquired through the Tucker-Davis Technologies (TDT) RZ10X Processor. Core packages include tdt (0.5.0) to read in the TDT RZ10X data, pandas (1.3.4) for data wrangling and creating data structures for analysis, numpy (1.20.3) and scipy (1.7.1) for mathematical and statistical operations, and matplotlib (3.4.3) and seaborn (0.11.2) for data visualization.

Fiber photometry signal processing

Fiber photometry signal data was low-pass filtered with a 3 Hz cut-off. Data in the 465 nm and 560 nm channels were then smoothed using a Savitzky-Golay (SG) filter with a 5 s window and detrended using Python's signal.detrend function to account for photobleaching. The 405 nm (isosbestic) channel was further low-pass filtered using scipy.signal.firwin with a 1 Hz cut-off, smoothed using the SG filter, and fitted to the 465 nm and 560 nm channels through ordinary least squares regression to remove motion artifacts. Then, 465 nm and 560 nm signals were z-scored using Python's stats.zscore function. For all state transition triggered averages in Figures 3.4.1,

3.4.2, and 3.4.4, the z-scored photometry signal was normalized by subtracting the mean of the signal during the pre-transition period.

EEG/EMG signal processing

EEG signals were detrended using a reverse exponential fit and large noise artifacts were deleted by z-scoring and clipping EEG signals > 8 standard deviations. Then manual inspection of EEG and EMG time frequency spectrograms was performed as quality control. When possible, easily identified noise artifacts were cut out from recordings. If EEG or EMG recordings were excessively contaminated with noise, the electrophysiology and accompanying fiber photometry recording were removed from final datasets.

Sleep/wake analysis

For sleep scoring, multi-taper spectral analysis (number of tapers = 29; window = 30 s; step size = 1 s) of EEG data[111] was used to determine average delta (0.5–4 Hz) power over time to train a Hidden Markov Model (hmmlearn, GitHub) to infer NREM and wake states, in each recording. In the HMM model, wake and NREM periods were scored with 1 and 0, respectively. To identify behavioral states with high confidence, 100 iterations of the HMM were averaged and then NREM and wake bouts were identified based on HMM scores across the EEG recording (NREM < 0.45; wake > 0.55) and bout length (NREM ≥ 100s and wake ≥ 30s). From the predicted wake states, EMG data (when available), was incorporated to determine REM states based on low EMG power across 65-100 Hz. When EMG was not available, REM bouts were identified based on two criteria, 1) followed a NREM bout and 2) were ≤ 200 s. Using this method, 93-97% (Fig. 3.4.2 and Fig.

3.4.3) of each recording was scored as wake, NREM, or REM, leaving 3-7% of individual recordings with no wake, NREM, or REM designation.

For state dependent power spectral EEG analysis, multi-taper spectrograms (generated using parameters above) were separated into wake, NREM, or REM periods. Power spectral densities (PSD) for each state were then calculated by averaging power in the 1-20 Hz range for concatenated wake, NREM, and REM spectrogram periods. PSDs were normalized by total power acros 1-20 Hz in each state and displayed as a percentage. Relative band power in each state was similarly calculated for delta (1–4 Hz), (6-10 Hz), and sigma (10-15 Hz) frequency bands from the multi-taper spectrograms. Band powers were normalized to total power in each behavioral state.

3.5.4 Histology and immunohistochemistry

Mice were deeply anesthetized with vaporized isoflurane (1–1.5% vol.) and intracardially perfused with ~10 mL of ice-cold 1X PBS and then ~10 mL of ice-cold 4% PFA. The brain was carefully dissected out to preserve photometry fiber and EEG screw tracks and then fixed in 4% PFA overnight at 4°C, incubated in 30% sucrose at 4°C until no longer floating, frozen on dry ice and stored at -80°C. For slicing, the brain was brought to -20°C, embedded in OCT, and then coronally sectioned (40 μm) on a cryostat.

For antibody staining, sections were first washed 3x in 1X PBS and then permeabilized at R.T. in 0.01% TritonX in PBS for 30 minutes. Sections were blocked in 10% NGS (Invitrogen) for 1 hour at R.T. and then incubated O/N at 4°C in primary antibodies diluted in 2% NGS: 1:1000 chicken α GFP (Abcam, ab13970) for labelling Cre-GFP or GRAB-Ado, 1:1000 rat α mCherry (Invitrogen, M11217) for labelling jRGECO, and 1:1000 rabbit α GFAP or 1:250 rabbit α S100β (Sigma-Aldrich, SA-85500172) to label astrocytes. Next, sections were wash 3x in 1X PBS

before 2-hour R.T. incubation in secondary antibodies diluted in 2% NGS: 1:2000 goat α chicken 488 (Invitrogen, A11039), goat α rabbit 647 (Invitrogen, A21244), ± 1:2000 goat α rat 555 (Invitrogen, A21434). Finally, sections were washed 3x in 1X PBS, mounted in Fluoromount with DAPI, and coverslipped. Sections were imaged using confocal microscopy.

CHAPTER 4

IMPLICATIONS AND FUTURE DIRECTIONS

The experiments in this dissertation demonstrate that HA directly activates cortical astrocytes via H1R and suggest that astrocyte-H1R signaling shapes astrocyte Ca^{2+} dynamics and adenosine signaling specifically during REM sleep, when histaminergic neurons are quiet, and HA is therefore not released (Fig. 4.4.1). The synthesis of our *ex vivo* (Chapter 2) and *in vivo* (Chapter 3) results has major implications for how astrocytes integrate sleep/wake neuromodulators to contribute to arousal control, which are discussed and addressed via potential future experiments outlined below.

4.1 ASTROCYTIC INTEGRATION OF NEUROMODULATORS OVER LONG TIMECALES

Both *ex vivo* and *in vivo* results presented here suggest that H1R activity shapes astrocyte physiology even after the acute period of H1R stimulation. In *ex vivo* slice experiments, H1R activation reduced NE-triggered astrocyte Ca^{2+} elevations in WT astrocytes relative to H1R cKO astrocytes, even many minutes after the initial bath-application of HA. This aligns with our *in vivo* fiber photometry results which showed that H1R cKO mice exhibited more frequent Ca^{2+} spikes during wake, indicating that, under normal conditions, H1R signaling attenuates astrocyte Ca^{2+} responses to other wake-active neuromodulators, such as NE. Additionally, H1R deletion altered Ca^{2+} dynamics around NREM/REM state transitions, further supporting H1R-mediated modulation of Ca^{2+} responses to other inputs, given that HA release is low during NREM and even lower during REM[63]. Specifically, H1R deletion attenuated the Ca^{2+} increase at NREM-to-REM

transitions and the decrease at REM-to-NREM transitions. This could be explained by elevated baseline Ca^{2+} levels during NREM in H1R cKO mice, potentially reducing the gain of subsequent Ca^{2+} spikes during REM. Increased baseline Ca^{2+} during NREM in cKO mice aligns with the idea that H1R signaling dampens Ca^{2+} responses specifically to NE, which is released at low levels during NREM[112,113]. That said, baseline levels of Ca^{2+} activity are difficult to assess via z-scored fiber photometry analysis, but could be addressed in future experiments potentially via *in vivo* 2P-imaging.

Taken together, our *ex vivo* and *in vivo* results strongly suggest that H1R activity influences astrocyte physiology over extended timescales, modulating responses to non-histaminergic inputs. Possible underlying mechanisms include H1R-triggered changes in gene expression, protein phosphorylation, or receptor internalization that could, for example, shape Ca^{2+} responses to NE during wake or ACh during REM. H1R-dependent changes in gene expression could be assayed via cell-type specific RNA-sequencing. Or, in the case of assaying phosphorylation dynamics, astrocytes could be examined via phosphoproteomics. Using fluorescently tagged WT and H1R cKO astrocytes for cell sorting would facilitate such analyses. The effect of H1R activation could be further assessed by collecting cells during the active versus quiet phases of the murine circadian cycle, when HA release is high and low, respectively. These physiological profiling strategies could point to how H1R signaling shapes astrocyte responses to other neuromodulatory signals. It could also reveal H1R-sensitive pathways that shape purinergic signaling and other astrocyte functions known to regulate neuronal firing, such as glutamate uptake or K^+ homeostasis.

In summary, we emphasize that the effect of H1R on astrocyte functions might only be revealed when astrocytes are stimulated by a combination of inputs, such as HA alongside NE, or when astrocytes are assayed beyond the period of acute GPCR stimulation. Therefore, astrocyte

responses to neuromodulators, and downstream effects on neurons, should be studied on various timescales and in carefully considered neurophysiological contexts.

4.2 ASTROCYTIC REGUATION OF CORTICAL ADENOSINE DYNAMICS VIA NEUROMODULATORY SIGNALING

As with our Ca^{2+} data, the combination of *ex vivo* and *in vivo* results converge to suggest that astrocytic H1R plays a significant role in shaping purinergic signaling in the cortex. In *ex vivo* slice experiments, we found that HA drives a H1R-dependent, minutes-long delayed increase in ATP release, as seen in DA experiments that also revealed a minutes-long delayed increase in extracellular ATP post DA stimulation of Adra1a. The timing of our results is consistent with a recent study showing that optogenetic stimulation of astrocyte Ca^{2+} triggers astrocytic ATP release that peaks 5-10 minutes post stimulation[60]. It is tempting to suggest that the delayed ATP responses that we observed *ex vivo* align with our *in vivo* observation that astrocytic H1R deletion alters REM-specific extracellular adenosine dynamics, suggesting that HA released during wake may drive H1R-dependent changes in astrocytic ATP/adenosine release many minutes later during REM sleep. However, our experiments do not mechanistically link our *ex vivo* GRAB-ATP results and *in vivo* GRAB-Ado results. Considering the drastic differences in cellular physiology captured in acute slices versus the intact brain, it is possible that H1R modulation of ATP/adenosine release manifests differently in the two distinct experimental set ups. Future experiments will be necessary to determine if the hypothesized lysosomal ATP exocytosis mechanism (discussed in 2.3.2) underlies both our *ex vivo* and *in vivo* observations. That said, we can conclude that both *ex vivo* and *in vivo* experiments demonstrate that astrocyte-specific H1R deletion alters extracellular

ATP/adenosine dynamics in the neocortex, which strongly motivates further investigation into the underlying H1R-sensitive adenosine pathways and effects on circuit function.

The potential behavioral significance of H1R-mediated astrocyte-adenosine signaling lies in the fact that cortical adenosine dynamics are thought to be critical to arousal regulation, specifically in sleep homeostasis. Microdialysis studies have shown that extracellular adenosine builds up across wake periods in the cortex[28], which is confirmed by our GRAB-Ado photometry data. Additionally, adenosine receptor antagonists, such as caffeine, increase wakefulness and suppress sleep[44]. These results, along with the observation that local application of adenosine to the cortex promotes NREM sleep and increases delta power[29–31], indicate that extracellular adenosine in the cortex promotes sleep as a function of time awake, which is at the core of the sleep homeostat. Given that cortical astrocytes express wake-active neuromodulatory receptors such H1R—which could couple astrocyte activity to time spent awake—and astrocytes' ability to increase extracellular adenosine levels, cortical astrocyte-neuromodulatory signaling likely plays a role in adenosine-mediated sleep homeostasis. Our observation that astrocytic H1R shapes both adenosine dynamics and delta power, albeit during REM, strongly motivates investigating how astrocyte-specific H1R deletion shapes homeostatic changes in adenosine dynamics and SWA activity after sleep deprivation.

Considering cortical adenosine is known to promote delta oscillations during NREM sleep, we were surprised to find that decreased extracellular adenosine at REM-onset coincided with increased delta power throughout REM bouts. One possible explanation for this is that extracellular adenosine might have distinct effects on cortical circuit dynamics during different behavioral states, mirroring the differing combinations of neuromodulators that characterize wake, NREM, and REM. Alternatively, the observed change in adenosine dynamics may not mediate the

change in REM-specific delta power, instead this could be dependent on other astrocyte outputs yet to be tested. Given that very little is known about how cortical astrocytes contribute to REM-sleep control, our findings set an important precedent for more focused investigation into how astrocyte signaling, specifically via neuromodulators, regulate REM dynamics.

4.3 SUMMARY

Our findings establish a compelling link between H1R modulation of astrocytic Ca^{2+} and two critical regulators of arousal: extracellular adenosine and cortical SWA. This aligns with past studies demonstrating that astrocytic Ca^{2+} activity and regulation of adenosine can drive changes in sleep/wake and underlying cortical oscillations, as well as those showing that astrocyte-neuromodulatory signaling shapes extracellular adenosine levels. By placing H1R at the center of these interactions, our work highlights H1R as a pivotal target for investigating astrocyte-mediated arousal control (Fig. 4.4.1).

Several key questions emerge from this work. For instance, how does astrocyte-specific H1R shape extracellular adenosine signaling and SWA after sleep deprivation? What other astrocyte outputs might H1R regulate to ultimately shape neuronal dynamics during REM sleep? How does astrocyte H1R signaling shape local neuronal activity, as measured by local field potentials or single-cell recordings? Furthermore, how do other neuromodulatory GPCRs interact with H1R to coordinate astrocytic arousal control? Addressing these questions will advance our understanding of astrocyte-neuromodulatory interactions in arousal regulation.

Understanding how different neuromodulators distinctly and synergistically control astrocytic arousal control—particularly via adenosine signaling—will provide a more comprehensive

understanding of how neuromodulators influence neuronal dynamics across sleep/wake. This knowledge could reveal new therapeutic targets for attentional and sleep disorders.

4.4 FIGURES

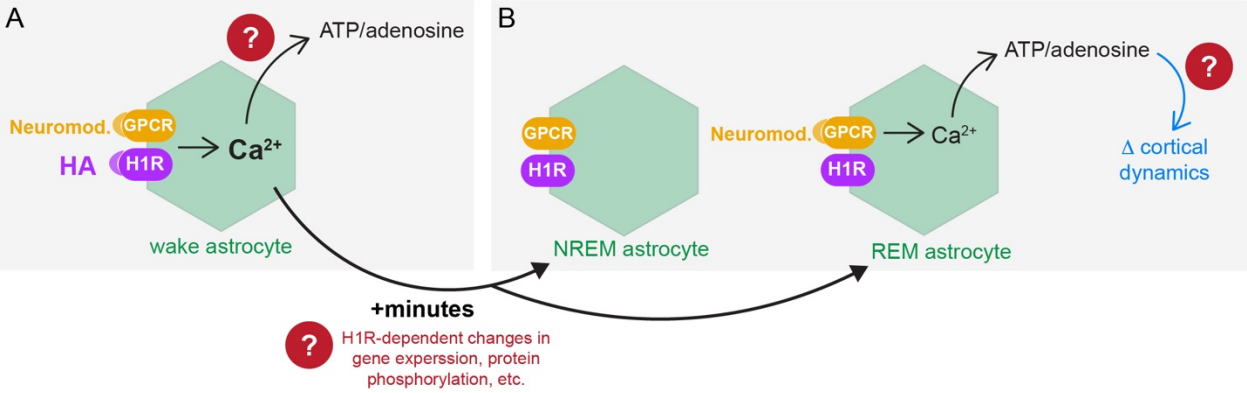

Figure 4.4.1. Dissertation summary schematic.
(A) Schematized wake-specific astrocyte responds to HA and other neuromodulators with high Ca^{2+} activity and ATP/adenosine release. Question mark (red) above astrocyte indicates unknown causal relationship between neuromodulator-triggered Ca^{2+} and ATP/adenosine release. Lower question mark indicates working hypothesis that H1R-triggered Ca^{2+} drives unknown long-lasting cellular changes that shape astrocytic responses to non-histaminergic inputs, potentially during NREM and REM (black solid arrows). **(B)** Schematized NREM- and REM-specific astrocytes. Few H1R-dependent changes were observed in NREM astrocytes. REM astrocytes exhibit H1R-sensitive Ca^{2+} responsiveness and ATP/adenosine regulation. Question mark indicates unknown relationship between observed H1R-dependent changes in extracellular adenosine and delta power during REM.

REFERENCES

1. Sulaman, B. A., Wang, S., Tyan, J. & Eban-Rothschild, A. Neuro-orchestration of sleep and wakefulness. *Nat Neurosci* 26, 196–212 (2023).
2. R. Zielinski, M., T. McKenna, J. & W. McCarley, R. Functions and Mechanisms of Sleep. *AIMS Neurosci* 3, 67–104 (2016).
3. Brown, R. E., Basheer, R., McKenna, J. T., Strecker, R. E. & McCarley, R. W. Control of sleep and wakefulness. *Physiol Rev* 92, 1087–187 (2012).
4. Walker, M. P. Cognitive consequences of sleep and sleep loss. *Sleep Med* 9, (2008).
5. Krystal, A. D. Psychiatric Disorders and Sleep. *Neurol Clin* 30, 1389–1413 (2012).
6. Lee, S. H. & Dan, Y. Neuromodulation of Brain States. *Neuron* 76, 209–222 (2012).
7. McCormick, D. A., Nestvogel, D. B. & He, B. J. Neuromodulation of Brain State and Behavior. *Annu Rev Neurosci* 43, 391–415 (2020).
8. Farhy-Tselnicker, I. *et al.* Activity-dependent modulation of synapse-regulating genes in astrocytes. *Elife* 10, 1–43 (2021).
9. Zhang, Y. *et al.* An RNA-sequencing transcriptome and splicing database of glia, neurons, and vascular cells of the cerebral cortex. *Journal of Neuroscience* 34, 11929–11947 (2014).
10. Reitman, M. E. *et al.* Norepinephrine links astrocytic activity to regulation of cortical state. *Nat Neurosci* 26, 579–593 (2023).
11. Gordon, G. R. J. *et al.* Norepinephrine triggers release of glial ATP to increase postsynaptic efficacy. *Nat Neurosci* 8, 1078–1086 (2005).

12. Lefton, K. B. *et al.* Norepinephrine Signals Through Astrocytes To Modulate Synapses. *bioRxiv* 10.1101/2024.05.21.595135 Preprint at https://doi.org/10.1101/2024.05.21.595135 (2024).
13. Drummond, G. T. *et al.* Cortical norepinephrine-astrocyte signaling critically mediates learned behavior. Preprint at https://doi.org/10.1101/2024.10.24.620009 (2024).
14. Chen, A. B. *et al.* Norepinephrine changes behavioral state via astroglial purinergic signaling. *bioRxiv* 2024.05.23.595576 (2024).
15. Pittolo, S. *et al.* Dopamine activates astrocytes in prefrontal cortex via α1-adrenergic receptors. *Cell Rep* 40, 111426 (2022).
16. Verkhratsky, A. & Nedergaard, M. Physiology of Astroglia. *Physiol Rev* 98, 239–389 (2018).
17. Eban-Rothschild, A., Appelbaum, L. & de Lecea, L. Neuronal Mechanisms for Sleep/Wake Regulation and Modulatory Drive. *Neuropsychopharmacology* 43, 937–952 (2018).
18. Scammell, T. E., Arrigoni, E. & Lipton, J. O. Neural Circuitry of Wakefulness and Sleep. *Neuron* 93, 747–765 (2017).
19. Poulet, J. F. A. & Crochet, S. The cortical states of wakefulness. *Front Syst Neurosci* 12, 1–18 (2019).
20. Cooper, J. M., Halter, K. A. & Prosser, R. A. Circadian rhythm and sleep-wake systems share the dynamic extracellular synaptic milieu. *Neurobiol Sleep Circadian Rhythms* 5, 15–36 (2018).

21. Mao, R. *et al.* Behavioral and cortical arousal from sleep, muscimol-induced coma, and anesthesia by direct optogenetic stimulation of cortical neurons. *iScience* 27, 109919 (2024).

22. Saper, C. B., Fuller, P. M., Pedersen, N. P., Lu, J. & Scammell, T. E. Sleep State Switching. *Neuron* 68, 1023–1042 (2010).

23. Vyazovskiy, V. V. *et al.* Cortical Firing and Sleep Homeostasis. *Neuron* 63, 865–878 (2009).

24. Rodriguez, A. V. *et al.* Why does sleep slow-wave activity increase after extended wake? Assessing the effects of increased cortical firing during wake and sleep. *Journal of Neuroscience* 36, 12436–12447 (2016).

25. Timofeev, I. Origin of Slow Cortical Oscillations in Deafferented Cortical Slabs. *Cerebral Cortex* 10, 1185–1199 (2000).

26. Porkka-Heiskanen, T. & Kalinchuk, A. V. Adenosine, energy metabolism and sleep homeostasis. *Sleep Med Rev* 15, 123–135 (2011).

27. Porkka-Heiskanen, T. *et al.* Adenosine: A mediator of the sleep-inducing effects of prolonged wakefulness. *Science (1979)* 276, 1265–1267 (1997).

28. Porkka-Heiskanen, T., Strecker, R. E. & McCarley, R. W. Brain site-specificity of extracellular adenosine concentration changes during sleep deprivation and spontaneous sleep: An in vivo microdialysis study. *Neuroscience* 99, 507–517 (2000).

29. Pethő, M. *et al.* Region-specific adenosinergic modulation of the slow-cortical rhythm in urethane-anesthetized rats. *Brain Res* 1725, 146471 (2019).

30. Van Dort, C. J., Baghdoyan, H. A. & Lydic, R. Adenosine A1 and A2A receptors in mouse prefrontal cortex modulate acetylcholine release and behavioral arousal. *Journal of Neuroscience* 29, 871–881 (2009).

31. Zhou, X. *et al.* 40 Hz light flickering promotes sleep through cortical adenosine signaling. *Cell Res* 34, 214–231 (2024).

32. Vizi, E. S., Kiss, J. P. & Lendvai, B. Nonsynaptic communication in the central nervous system. *Neurochem Int* 45, 443–451 (2004).

33. Jacob, S. N. & Nienborg, H. Monoaminergic Neuromodulation of Sensory Processing. *Front Neural Circuits* 12, 1–17 (2018).

34. Berridge, C. W. & Waterhouse, B. D. The locus coeruleus–noradrenergic system: modulation of behavioral state and state-dependent cognitive processes. *Brain Res Rev* 42, 33–84 (2003).

35. Pacholko, A. G., Wotton, C. A. & Bekar, L. K. Astrocytes—The Ultimate Effectors of Long-Range Neuromodulatory Networks? *Front Cell Neurosci* 14, 1–12 (2020).

36. Hirase, H., Iwai, Y., Takata, N., Shinohara, Y. & Mishima, T. Volume transmission signalling via astrocytes. *Philosophical Transactions of the Royal Society B: Biological Sciences* 369, 20130604 (2014).

37. Ingiosi, A. M. & Frank, M. G. Goodnight, astrocyte: waking up to astroglial mechanisms in sleep. *FEBS Journal* 290, 2553–2564 (2023).

38. Paukert, M. *et al.* Norepinephrine controls astroglial responsiveness to local circuit activity. *Neuron* 82, 1263–1270 (2014).

39. Ding, F. *et al.* α1-Adrenergic receptors mediate coordinated Ca2+ signaling of cortical astrocytes in awake, behaving mice. *Cell Calcium* 54, 387–394 (2013).

40. Oe, Y. *et al.* Distinct temporal integration of noradrenaline signaling by astrocytic second messengers during vigilance. *Nat Commun* 11, 471 (2020).

41. Poskanzer, K. E. & Yuste, R. Astrocytic regulation of cortical UP states. *Proc Natl Acad Sci U S A* 108, 18453–18458 (2011).

42. Poskanzer, K. E. & Yuste, R. Astrocytes regulate cortical state switching in vivo. *Proc Natl Acad Sci U S A* 113, E2675–E2684 (2016).

43. Vaidyanathan, T. V, Collard, M., Yokoyama, S., Reitman, M. E. & Poskanzer, K. E. Cortical astrocytes independently regulate sleep depth and duration via separate GPCR pathways. *Elife* 10, 1–55 (2021).

44. Lazarus, M., Oishi, Y., Bjorness, T. E. & Greene, R. W. Gating and the need for sleep: Dissociable effects of adenosine a1and a2areceptors. *Front Neurosci* 13, 1–12 (2019).

45. Frank, M. G. *The Role of Glia in Sleep-Wake Regulation and Function*. *Handbook of Behavioral Neuroscience* vol. 30 (Elsevier B.V., 2019).

46. Jha, P. K., Valekunja, U. K., Ray, S., Nollet, M. & Reddy, A. B. Single-cell transcriptomics and cell-specific proteomics reveals molecular signatures of sleep. *Commun Biol* 5, 846 (2022).

47. Bellesi, M., de Vivo, L., Tononi, G. & Cirelli, C. Effects of sleep and wake on astrocytes: Clues from molecular and ultrastructural studies. *BMC Biol* 13, 1–17 (2015).

48. Ingiosi, A. M. *et al.* A Role for Astroglial Calcium in Mammalian Sleep and Sleep Regulation. *Current Biology* 30, 4373-4383.e7 (2020).

49. Bojarskaite, L. *et al.* Astrocytic Ca2+ signaling is reduced during sleep and is involved in the regulation of slow wave sleep. *Nat Commun* 11, 3240 (2020).

50. Tsunematsu, T., Sakata, S., Sanagi, T., Tanaka, K. F. & Matsui, K. Region-Specific and State-Dependent Astrocyte Ca21 Dynamics during the Sleep-Wake Cycle in Mice. *Journal of Neuroscience* 41, 5440–5462 (2021).

51. Peng, W. *et al.* Adenosine-independent regulation of the sleep–wake cycle by astrocyte activity. *Cell Discov* 9, 16 (2023).

52. Ye, L. *et al.* Ethanol abolishes vigilance-dependent astroglia network activation in mice by inhibiting norepinephrine release. *Nat Commun* 11, 6157 (2020).

53. Bjorness, T. E. *et al.* An adenosine-mediated glial-neuronal circuit for homeostatic sleep. *Journal of Neuroscience* 36, 3709–3721 (2016).

54. Halassa, M. M. *et al.* Astrocytic Modulation of Sleep Homeostasis and Cognitive Consequences of Sleep Loss. *Neuron* 61, 213–219 (2009).

55. Fellin, T. *et al.* Endogenous nonneuronal modulators of synaptic transmission control cortical slow oscillations in vivo. *Proc Natl Acad Sci U S A* 106, 15037–15042 (2009).

56. Ian Schmitt, L., Sims, R. E., Dale, N. & Haydon, P. G. Wakefulness affects synaptic and network activity by increasing extracellular astrocyte-derived adenosine. *Journal of Neuroscience* 32, 4417–4425 (2012).

57. Fujita, T. *et al.* Neuronal transgene expression in dominant-negative snare mice. *Journal of Neuroscience* 34, 16594–16604 (2014).

58. Lalo, U. *et al.* Exocytosis of ATP From Astrocytes Modulates Phasic and Tonic Inhibition in the Neocortex. *PLoS Biol* 12, e1001747 (2014).

59. Lezmy, J. *et al.* Astrocyte Ca 2+ -evoked ATP release regulates myelinated axon excitability and conduction speed. *Science (1979)* 374, eabh2858 (2021).

60. Li, H. *et al.* Astrocytes release ATP/ADP and glutamate in flashes via vesicular exocytosis. *Mol Psychiatry* (2024) doi:10.1038/s41380-024-02851-8.

61. Illes, P., Burnstock, G. & Tang, Y. Astroglia-Derived ATP Modulates CNS Neuronal Circuits. *Trends Neurosci* 42, 885–898 (2019).

62. Corkrum, M. *et al.* Dopamine-Evoked Synaptic Regulation in the Nucleus Accumbens Requires Astrocyte Activity. *Neuron* 105, 1036-1047.e5 (2020).

63. Dong, H. *et al.* Genetically encoded sensors for measuring histamine release both in vitro and in vivo. *Neuron* 111, 1564-1576.e6 (2023).

64. Lin, J. S. Brain structures and mechanisms involved in the control of cortical activation and wakefulness, with emphasis on the posterior hypothalamus and histaminergic neurons. *Sleep Med Rev* 4, 471–503 (2000).

65. Chu, M. *et al.* Extracellular histamine level in the frontal cortex is positively correlated with the amount of wakefulness in rats. *Neurosci Res* 49, 417–420 (2004).

66. Takahashi, K., Lin, J. S. & Sakai, K. Neuronal activity of histaminergic tuberomammillary neurons during wake-sleep states in the mouse. *Journal of Neuroscience* 26, 10292–10298 (2006).

67. Lin, W. *et al.* Whole-brain mapping of histaminergic projections in mouse brain. *Proc Natl Acad Sci U S A* 120, e2216231120 (2023).

68. Haas, H. & Panula, P. The role of histamine and the tuberomamillary nucleus in the nervous system. *Nat Rev Neurosci* 4, 121–130 (2003).

69. White, J. M. & Rumbold, G. R. Behavioural effects of histamine and its antagonists: a review. *Psychopharmacology (Berl)* 95, 1–14 (1988).

70. Parmentier, R. *et al.* Role of histamine H1-receptor on behavioral states and wake maintenance during deficiency of a brain activating system: A study using a knockout mouse model. *Neuropharmacology* 106, 20–34 (2016).

71. Huang, Z.-L. *et al.* Altered sleep–wake characteristics and lack of arousal response to H 3 receptor antagonist in histamine H 1 receptor knockout mice. *Proceedings of the National Academy of Sciences* 103, 4687–4692 (2006).

72. Fujita, A. *et al.* Hypothalamic tuberomammillary nucleus neurons: Electrophysiological diversity and essential role in arousal stability. *Journal of Neuroscience* 37, 9574–9592 (2017).

73. Monti, J. M., Pellejero, T. & Jantos, H. Effects of H1- and H2-histamine receptor agonists and antagonists on sleep and wakefulness in the rat. *J Neural Transm* 66, 1–11 (1986).

74. Gondard, E. *et al.* Enhanced histaminergic neurotransmission and sleep-wake alterations, a study in histamine H3-receptor knock-out mice. *Neuropsychopharmacology* 38, 1015–1031 (2013).

75. Lucaci, D., Yu, X., Chadderton, P., Wisden, W. & Brickley, S. G. Histamine Release in the Prefrontal Cortex Excites Fast-Spiking Interneurons while GABA Released from the Same Axons Inhibits Pyramidal Cells. *Journal of Neuroscience* 43, 187–198 (2023).

76. Panula, P. & Nuutinen, S. The histaminergic network in the brain: basic organization and role in disease. *Nat Rev Neurosci* 14, 472–487 (2013).

77. Hösli, E. & Hösli, L. Autoradiographic localization of binding sites for [3H]histamine and H1- and H2-antagonists on cultured neurones and glial cells. *Neuroscience* 13, 863–870 (1984).

78. Jurič, D. M., Kržan, M. & Lipnik-Stangelj, M. Histamine and astrocyte function. *Pharmacol Res* 111, 774–783 (2016).

79. Kárpáti, A. *et al.* Histamine H1 receptor on astrocytes and neurons controls distinct aspects of mouse behaviour. *Sci Rep* 9, 3–4 (2019).

80. Pryazhnikov, E. & Khiroug, L. Sub-micromolar increase in [Ca 2+] i triggers delayed exocytosis of ATP in cultured astrocytes. *Glia* 56, 38–49 (2008).

81. Zhang, Z. *et al.* Regulated ATP release from astrocytes through lysosome exocytosis. *Nat Cell Biol* 9, 945–953 (2007).

82. Lezmy, J. How astrocytic ATP shapes neuronal activity and brain circuits. *Curr Opin Neurobiol* 79, 102685 (2023).

83. Slezak, M. *et al.* Distinct Mechanisms for Visual and Motor-Related Astrocyte Responses in Mouse Visual Cortex. *Current Biology* 29, 3120-3127.e5 (2019).

84. Kirischuk, S., Tuschick, S., Verkhratsky, A. & Kettenmann, H. Calcium Signalling in Mouse Bergmann Glial Cells Mediated by α 1 -adrenoreceptors and H 1 Histamine - Receptors. *European Journal of Neuroscience* 8, 1198–1208 (1996).

85. Wang, Y. *et al.* Accurate quantification of astrocyte and neurotransmitter fluorescence dynamics for single-cell and population-level physiology. *Nat Neurosci* 22, 1936–1944 (2019).

86. Cahill, M. K. *et al.* Network-level encoding of local neurotransmitters in cortical astrocytes. *Nature* 629, 146–153 (2024).

87. Leenaars, C. H. C. *et al.* Sleep and microdialysis: An experiment and a systematic review of histamine and several amino acids. *J Circadian Rhythms* 17, 1–12 (2019).

88. Samaranayake, S. *et al.* In vivo histamine voltammetry in the mouse premammillary nucleus. *Analyst* 140, 3759–3765 (2015).

89. Berger, S. N. *et al.* An In Vivo Definition of Brain Histamine Dynamics Reveals Critical Neuromodulatory Roles for This Elusive Messenger. *Int J Mol Sci* 23, (2022).

90. Shelton, M. K. & McCarthy, K. D. Hippocampal Astrocytes Exhibit Ca 2+ -Elevating Muscarinic Cholinergic and Histaminergic Receptors In Situ. *J Neurochem* 74, 555–563 (2000).

91. Xia, P., Logiacco, F., Huang, Y., Kettenmann, H. & Semtner, M. Histamine triggers microglial responses indirectly via astrocytes and purinergic signaling. *Glia* 69, 2291–2304 (2021).

92. Casper, K. B. & McCarthy, K. D. GFAP-positive progenitor cells produce neurons and oligodendrocytes throughout the CNS. *Molecular and Cellular Neuroscience* 31, 676–684 (2006).

93. Mamber, C. *et al.* GFAPδ Expression in Glia of the Developmental and Adolescent Mouse Brain. *PLoS One* 7, 1–15 (2012).

94. Bekar, L. K., He, W. & Nedergaard, M. Locus Coeruleus α-Adrenergic–Mediated Activation of Cortical Astrocytes In Vivo. *Cerebral Cortex* 18, 2789–2795 (2008).

95. Pankratov, Y. & Lalo, U. Role for astroglial α1-adrenoreceptors in gliotransmission and control of synaptic plasticity in the neocortex. *Front Cell Neurosci* 9, 1–11 (2015).

96. Wahis, J. *et al.* The astrocyte α1A-adrenoreceptor is a key component of the neuromodulatory system in mouse visual cortex. *Glia* 1955–1973 (2024) doi:10.1002/glia.24591.

97. Wu, Z. *et al.* A sensitive GRAB sensor for detecting extracellular ATP in vitro and in vivo. *Neuron* 110, 770-782.e5 (2022).

98. Rasmussen, R. N., Asiminas, A., Carlsen, E. M. M., Kjaerby, C. & Smith, N. A. Astrocytes: integrators of arousal state and sensory context. *Trends Neurosci* 46, 418–425 (2023).

99. Courjaret, R., Dib, M. & Machaca, K. Spatially restricted subcellular Ca2+ signaling downstream of store-operated calcium entry encoded by a cortical tunneling mechanism. *Sci Rep* 8, 1–13 (2018).

100. Guttenplan, K. A. *et al.* Adrenergic signaling gates astrocyte responsiveness to neurotransmitters and control of neuronal activity. 1–25 Preprint at https://doi.org/10.1101/2024.09.23.614537 (2024).

101. Lyon, K. A. & Allen, N. J. From Synapses to Circuits, Astrocytes Regulate Behavior. *Front Neural Circuits* 15, (2022).

102. Pascual, O. *et al.* Neurobiology: Astrocytic purinergic signaling coordinates synaptic networks. *Science (1979)* 310, 113–116 (2005).

103. Wu, Z. *et al. A GRAB Sensor Reveals Activity-Dependent Non-Vesicular Somatodendritic Adenosine Release*. *bioRxiv* (2020). doi:10.1101/2020.05.04.075564.

104. Peng, W. *et al.* Regulation of sleep homeostasis mediator adenosine by basal forebrain glutamatergic neurons. *Science (1979)* 369, (2020).

105. Srinivasan, R. *et al.* New Transgenic Mouse Lines for Selectively Targeting Astrocytes and Studying Calcium Signals in Astrocyte Processes In Situ and In Vivo. *Neuron* 92, 1181–1195 (2016).

106. Yu, X., Nagai, J. & Khakh, B. S. Improved tools to study astrocytes. *Nat Rev Neurosci* 21, 121–138 (2020).

107. Wang, Z. *et al.* REM sleep is associated with distinct global cortical dynamics and controlled by occipital cortex. *Nat Commun* 13, 1–17 (2022).

108. Miguel-Quesada, C. *et al.* Astrocytes adjust the dynamic range of cortical network activity to control modality-specific sensory information processing. *Cell Rep* 42, 112950 (2023).

109. Porkka-Heiskanen, T. Adenosine in sleep and wakefulness. *Ann Med* 31, 125–129 (1999).

110. Liang, Y. W. *et al.* Experimental Verification for Numerical Simulation of Thalamic Stimulation-Evoked Calcium-Sensitive Fluorescence and Electrophysiology with Self-Assembled Multifunctional Optrode. *Biosensors (Basel)* 13, (2023).

111. Prerau, M. J., Brown, R. E., Bianchi, M. T., Ellenbogen, J. M. & Purdon, P. L. Sleep neurophysiological dynamics through the lens of multitaper spectral analysis. *Physiology* 32, 60–92 (2017).

112. Kjaerby, C. *et al.* Memory-enhancing properties of sleep depend on the oscillatory amplitude of norepinephrine. *Nat Neurosci* 25, 1059–1070 (2022).

113. Osorio-Forero, A. *et al.* Noradrenergic locus coeruleus activity functionally partitions NREM sleep to gatekeep the NREM-REM sleep cycle. *bioRxiv* 2023.05.20.541586 (2024) doi:10.1038/s41593-024-01822-0.

Publishing Agreement

It is the policy of the University to encourage open access and broad distribution of all theses, dissertations, and manuscripts. The Graduate Division will facilitate the distribution of UCSF theses, dissertations, and manuscripts to the UCSF Library for open access and distribution. UCSF will make such theses, dissertations, and manuscripts accessible to the public and will take reasonable steps to preserve these works in perpetuity.

I hereby grant the non-exclusive, perpetual right to The Regents of the University of California to reproduce, publicly display, distribute, preserve, and publish copies of my thesis, dissertation, or manuscript in any form or media, now existing or later derived, including access online for teaching, research, and public service purposes.

DocuSigned by:
Charlotte Taylor
FD7B80CE3A104A5...
Author Signature

12/12/2024
Date